Solar Energy 314 (2026) 114687

Contents lists available at ScienceDirect

Solar Energy

journal homepage: www.elsevier.com/locate/solener

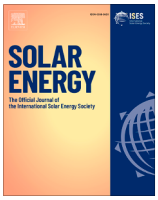

Worldwide benchmarking of cost-effective radiometers for direct and diffuse irradiance

Niklas Blum [a,*], Bijan Nouri [a], Yann Fabel [a], Laura Campos Guzmán [a], Jonas Stührenberg [b], Andreas Kazantzidis [c], Mounir Abraim [d], Martina Calais [e], Aron Habte [f], Anne Forstinger [g], Felix Maas [a], Rafal Broda [a], Paul Matteschk [a], Luis F. Zarzalejo [h], Orestis Panagopoulos [c], Abdellatif Ghennioui [d], Stefan Wilbert [a]

[a] German Aerospace Center (DLR), Institute of Solar Research, Calle Doctor Carracido 44, Almería, 04005, Andalucía, Spain
[b] German Aerospace Center (DLR), Institute of Networked Energy Systems, Carl-von-Ossietzky-Str. 15, Oldenburg, 26129, Lower Saxony, Germany
[c] University of Patras, Department of Physics, Laboratory of Atmospheric Physics, Patras, 26500, Greece
[d] Green Energy Park Research Platform (GEP, IRESEN/UM6P), Route Régionale R206, Benguerir, Morocco
[e] Murdoch University, School of Engineering and Energy, College of Science, Technology, Engineering and Mathematics, 90 South St, Murdoch, WA 6150, Western Australia, Australia
[f] National Renewable Energy Laboratory (NREL), Power Systems Engineering Center, Golden, Colorado CO 80401, United States
[g] CSP Services GmbH, Friedrich-Ebert-Ufer 30, Cologne, 51143, Germany
[h] CIEMAT Energy Department, Renewable Energy Division, Avenida Complutense 40, Madrid, 28040, Madrid, Spain

HIGHLIGHTS

- Accuracy of practically feasible sensors for direct and diffuse irradiance evaluated.
- EKO MS-90, Delta-T SPN1, RSI/RSP, PyranoCam, Sunto CaptPro, Kipp & Zonen CSD3 tested.
- Six sites worldwide included with approximately one year of measurements per site.
- Influences of atmospheric and site conditions on the sensors' accuracies investigated.
- Strong differences in accuracy found between the radiometer types.

ARTICLE INFO

Keywords:
Circumsolar irradiance
Sensor comparison
Accuracy
Uncertainty
Shortwave radiation
Pyranometer

ABSTRACT

Solar energy projects can benefit from direct normal irradiance (DNI) and diffuse horizontal irradiance (DHI) measurements during all project phases. Several commercial measurement systems for DNI and DHI are available. Sun trackers with pyranometers and pyrheliometers can provide highly accurate measurements but are often impractical in solar energy applications. For less expensive and more robust sensors, it is often unclear which accuracy can be expected under a project site's specific atmospheric conditions. We address this challenge through our dedicated experimental comparison of relevant sensor systems (rotating shadowband irradiometer [short RSI], Delta-T SPN1, EKO MS-90, PyranoCam, Sunto CaptPro, Kipp & Zonen CSD3) at up to six sites worldwide. The RSI systems (*rRMSD* 3 to 8.6%, DNI; 4.8 to 7.6%, DHI) and PyranoCam (*rRMSD* 2.6 to 5.2%, DNI; 4.4 to 5.8%, DHI) exhibit similar error metrics and are the most accurate systems in the test. Delta-T SPN1 and EKO MS-90 (*rRMSD* 6.8 to 15%, DNI; 10.6 to 20.1%, DHI) but especially Kipp & Zonen CSD3 and Sunto CaptPro show significant deviations (*rRMSD* 17.7 to 20%, DNI; 33 to 58%, DHI). We evaluate the influence of relevant atmospheric parameters on the sensors' accuracies by a rather unique measurement setup. MS-90's DNI errors depend on DNI itself, with overestimations for low reference DNI. The deviations of SPN1's DHI and DNI measurements increase sharply in situations with high circumsolar irradiance. Also CaptPro and CSD3's increased measurement errors are related to circumsolar irradiance. For RSI and PyranoCam, only moderate influences on the measurements are identified, indicating a general applicability of these instruments.

* Corresponding author.
Email address: Niklas.Blum@dlr.de (N. Blum).

https://doi.org/10.1016/j.solener.2026.114687
Received 14 October 2025; Received in revised form 14 April 2026; Accepted 4 May 2026
Available online 9 May 2026
0038-092X/© 2026 The Authors. Published by Elsevier Ltd on behalf of International Solar Energy Society. This is an open access article under the CC BY license (http://creativecommons.org/licenses/by/4.0/).

Fig. 2. Overview of the measurement setups in Tabernas at CIEMAT's Plataforma Solar de Almería (top), Oldenburg (center), Patras (bottom, left), Benguerir (bottom, center) and Perth (bottom, right). The setup in Golden (for pictures and further information, see [25]) is not shown.

range of 300 to 1700 nm with a spectral resolution < 7 nm. These spectra are extrapolated to the full broadband range (280 to 4000 nm) by the method of Anderson [27], modeling all-sky-irradiance spectra according to Jessen et al. [28], based on SMARTS [29] clear-sky spectra, the current atmospheric conditions indicated by AERONET [30] and cloud attenuation from the SEDES2 [31] model. The spectroradiometers were located at a distance of 840 m from the remaining measurement setup.

A special setup was developed to measure circumsolar irradiance (shown in Fig. 2, top on the very right). The setup consists of two shaded and tracked pyranometers in a sun-normal plane. The circular shades were designed to obscure sun distance angles up to 2.5° and 5°, respectively. The distance between the shades and pyranometers and the resulting shade diameters were chosen to comply with the shading geometry of diffusometers and pyrheliometers described by Major [32]. The penumbra function of the 2.5° shade reproduces the ones of a CHP1 and absolute cavity pyrheliometer as far as possible while meeting the condition that the entire glass dome of the pyranometer should be shaded. The two pyranometers' measurements are subtracted to yield the circumsolar irradiance from sun distance angles between 2.5° and 5°. A more detailed description of this measurement setup is given in Appendix A. A related setup was used by Badosa et al. [18] to investigate the influence of circumsolar irradiance on SPN1's DHI measurement. In that case, two pyranometers were placed in the horizontal plane and shaded with shading disks corresponding to sun distance angles of 2.5 (regular DHI measurement) and 6.5°. In the present study, the pyranometers were placed in a sun-normal plane to receive a constant shading geometry at all sun elevation angles (see [32]).

2.3. Data acquisition and processing

The following procedures were applied in the acquisition and processing of the measurement data. All radiometers were cleaned on weekdays in Tabernas and weekly at the other locations. All measurements were checked semi-automatically by an expert using the procedure of Geuder et al. [33]. Automatic filters, including the three-component test, supported the expert in checking the reference data. Additionally, measurements of the same parameter were compared between the instruments to detect deviations resulting from disturbances such as shading. Only data points that passed all filters and corresponded to a sun elevation of at least 5° were used in the evaluations of this study.

All evaluated test systems were calibrated using the reference sensors at the respective site. The measurement periods of calibration and testing

Table 2
Summary of the calibration applied to each test sensor. At least one parameter (GHI, DHI, DNI) is calibrated by comparison to the respective reference measurement. CSD3, MS-90 and PyranoCam receive GHI from the unshaded thermopile pyranometer. All GHI measurements are calibrated relative to GHI calculated from DNI and DHI. Each sensor calculates either DHI or DNI from two already calibrated measurements. No additional calibration is applied to the calculated parameter.

	GHI	DHI	DNI
MS-90	calibrated	–	calibrated
CSD3	calibrated	–	calibrated
SPN1	calibrated	constant from GHI	–
RSI	calibrated	calibrated	–
PyranoCam	calibrated	calibrated	–
CaptPro	–	calibrated	calibrated

Table 3
Sampling times of the test sensors used in the data acquisition. All measurement data were saved as 1-min averages after data acquisition.

	GHI	DHI	DNI
MS-90	1 s	–	15 s
CSD3	1 s	–	1 s
SPN1	1 s	1 s	–
RSP (Tabernas)	1 s	60 s	–
RSI (other sites)	1 s	30 s	–
PyranoCam	1 s	30 s	–
CaptPro	1 s	1 s	1 s

are shown in Table 1. At all sites where a sensor comparison was performed (Tabernas, Oldenburg, Golden, Patras), a measurement period of twelve months was realized and one of these twelve months was reserved for calibrating the test sensors. The start date of the respective measurement period was determined by the availability of personnel and hardware at the respective site. At the two additional sites, where only PyranoCam was tested (Benguerir, Perth), the measurement period was chosen to be as long as possible given practical considerations such as outages of the reference measurements and the availability of personnel for maintenance and data checks. For PyranoCam and RSI, an evaluation without onsite calibration was also performed. During the calibration, the final measurements from each test instrument were scaled by a constant factor to achieve the same mean irradiance from both, the test and reference measurement, over all data points of the calibration period that corresponded to a sun elevation of at least 10°. Table 2 summarizes which parameters of each sensor were calibrated. For SPN1, the same calibration constant was applied for GHI and DHI as the same sensors measure both variables.

The sensor planes of all measurement systems were arranged at the same height as far as possible. Shading by surrounding objects was avoided as much as possible. Periods during which individual instruments were still shaded were filtered out during the data checks.

The data loggers at the respective locations were always synchronized via NTP (Network Time Protocol). Measurement data were sampled at 1-s resolution and recorded as 1-min averages. The sampling times of the test sensors' parameters were in part larger due to the respective measurement principles, as shown in Table 3.

3. Tested instruments

The characteristics of each tested measurement system are summarized briefly in the following. These rather inexpensive systems usually measure two of the parameters GHI, DNI and DHI and calculate the third one. The following closure equation provides the third parameter with the solar elevation angle, α:

$$GHI = DHI + DNI \cdot \sin(\alpha) \tag{1}$$

Fig. 3. Images of the SPN1 and RSP operated in Tabernas at CIEMAT's PSA.

3.1. Delta-T SPN1

The SPN1 Sunshine Pyranometer from Delta-T (shown in Fig. 3, left) uses seven thermopile pyranometers arranged under a special shadow mask to calculate GHI and DHI. The shadow mask is designed to obscure 50% of the sky hemisphere in each pyranometer's field of view. Additionally, at any given time the sun disk is completely obscured for at least one of the pyranometers and unobscured for at least one other. Assuming an isotropic distribution of the diffuse radiation over the entire sky hemisphere, GHI and DHI are calculated as follows from the measured irradiances, $Irrad_i$, of the seven pyranometers [34]:

$$DHI = 2 \min_{i \in \{1,2,\ldots,7\}} Irrad_i \tag{2}$$

$$GHI = \min_{i \in \{1,2,\ldots,7\}} Irrad_i + \max_{i \in \{1,2,\ldots,7\}} Irrad_i \tag{3}$$

The assumption of isotropic diffuse radiation is a strong simplification. In particular, circumsolar and horizon brightening are common phenomena influenced by turbidity and cloud cover, among other parameters [35]. In addition, SPN1's thermopile pyranometers have a spectral range of 400 to 2700 nm which does not cover the entire wavelength range of shortwave radiation (280 to 3000 nm). This may cause further measurement errors under some conditions [18]. Accordingly, previous studies have shown that the SPN1 can introduce significant deviations depending on the turbidity and cloudiness of the atmosphere and the sun position, in particular regarding the azimuth angle [16–18].

3.2. Rotating shadowband irradiometers

The rotating shadowband irradiometers (RSIs) tested in this study represent different models and manufacturers: Reichert RSP-4G, CSP Services Twin RSI, Irradiance Inc. RSP v2, each using a LI-COR LI-200 pyranometer. RSP-4G is shown in Fig. 3 (right). These instruments use almost the same measurement setup. A photodiode pyranometer measures GHI. A shadowband rotates regularly with a repetition frequency of 30 s or 60 s and shades the pyranometer for a short period. During this period, the measurement signal collapses and the respective minimum corresponds to DHI (see [36] for details). The measurement principle requires a radiation sensor with a very short response time, which is why photodiode pyranometers are used. These sensors have a limited spectral range of around 400 to 1100 nm. In addition, their spectral sensitivity is very nonuniform and reaches its maximum at around 950 nm [37].

RSIs exhibit in particular the following sources of error: spectral response, zenith angle response, calibration uncertainty and temperature response [38,39]. Since the spectral compositions of GHI and DHI vary greatly with atmospheric conditions, spectral correction functions have been developed, e.g., [40–42]. Even after applying such correction functions, notable spectral errors can persist [16,17,38]. The calibration and correction functions of Geuder et al. [40] were applied to the RSI sensors in Tabernas, Oldenburg and Patras. Measurements from the RSP in Golden were corrected via the manufacturer's firmware. Kern [43] and King et al. [42,44] provide some information on the corrections applied by the Irradiance RSP. In summary, each RSI (including RSP)

Fig. 4. Left: MS-90 operated in Tabernas at CIEMAT's PSA. Right: Exemplary photo of a CSD3 in the field.

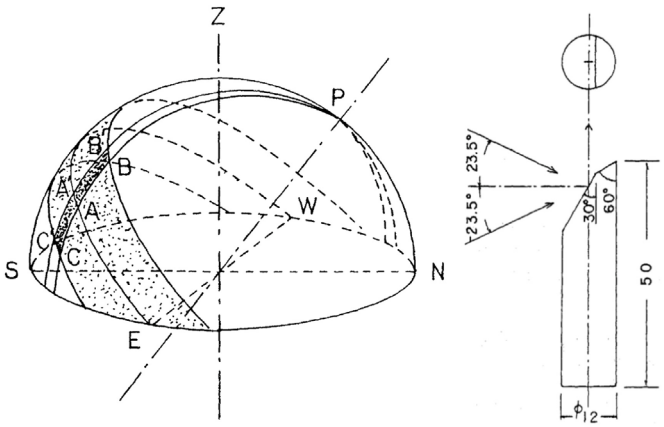

Fig. 5. Left: Visualization of the MS-90's expected field of view (FOV), represented by the dark shaded area with the corner points B, B', C', C, at a given point in time. The figures are taken from [45] and are based on a predecessor model of the MS-90. The figure corresponds to a measurement in the Northern Hemisphere. The FOV is determined by the optical properties of the mirror (right). It covers a solid angle of 0.2 sr and has the 'side lengths' 90° (B-C) and 8° (A-A'). As the mirror rotates around the axis P, which is tilted by the local latitude angle over the North-South axis, the FOV moves through the shaded spherical sector of the sky dome. This way, the FOV includes the sun disk for a short period in each rotation (every 15 s). Figure reproduced from [45] with permission by the Meteorological Society of Japan.

instrument tested in this study applies correction functions that account for the above-mentioned sources of error.

3.3. EKO MS-90

EKO MS-90 (shown in Fig. 4, left) is based on a sunshine duration sensor concept and measures DNI [20]. The sensor's measurement principle is similar to those of the EKO MS-93 and other predecessors that have been described and validated in the literature (e.g., [45,46]). A special mirror rotates with a period of 15 s. Due to the unique shape and surface structure of the mirror, radiation from a certain field of view (FOV) is projected onto a pyroelectric sensor. While the sensor's FOV is not precisely known, it can be derived qualitatively from a predecessor model [45], as shown in Fig. 5. The FOV is marked by the corner points B, B', C', C. As the mirror rotates, the FOV moves through the shaded spherical sector. If the measuring device is correctly aligned, this spherical sector always contains the sun disk. The MS-90's pyroelectric sensor generates a measurement signal that is directly related to a transient in the received radiation. Thus, the inhomogeneous radiation distribution within the spherical sector shown in Fig. 5 and particularly the presence of direct irradiance cause the measurement signal. The maximum measurement signal per time interval of 15 s is then multiplied by a calibration constant to obtain DNI. Similar to thermopile instruments, the pyroelectric sensor transforms radiation into heat and measures a resulting temperature change [20]. Accordingly, the manufacturer specifies a broad spectral range of 300 to 2700 nm [47]. In combination with GHI measured by a thermopile pyranometer, DHI is calculated.

In clear conditions, previous investigations of the MS-90 have shown an acceptable accuracy of the measured DNI with relative deviations in the range of ±5% (interquartile range) [19,20]. Compared to clear conditions, the MS-90 can introduce increased deviations of the measured DNI in other conditions, e.g., in cloudy or more turbid conditions [19,20]. The study of Pó et al. [20] suggested a strong relationship between the MS-90's measurement deviation and reference DNI. With decreasing reference DNI, the MS-90 increasingly overestimates DNI, approaching a relative overestimation of 20% at a reference DNI of 200 W/m^2.

Due to the measurement principle, only one measured value (sample) of the DNI is obtained every 15 s. This can lead to increased measurement errors if a high time resolution is evaluated under variable conditions, e.g., with broken cloud cover. At this point, note that DNI is by far more variable than DHI at timescales of 1 min and below. This intuitive circumstance was found, e.g., in a case study for Singapore [48] and in the present study, as will be discussed in more detail in Section 5.1.2.

It was observed that the MS-90 can cause systematic errors in the measured DNI depending on the time of year, which are small at the equinox, but more pronounced in summer and winter [19]. This can be explained by the fact that the sensor is typically operated throughout the year at an unchanged inclination. Apparently, the sensor's sensitivity depends to some degree on the angle between the sun rays and the MS-90's rotation axis. This effect was also described in [45]. Additionally, the sensor's sensitivity may change by up to ±5% if the ambient temperature varies within −20 to 40 °C [45,47]. When determining DHI from the MS-90's DNI and the pyranometer's GHI, note that moderate relative errors (e.g., calibration errors) can amplify when subtracting these signals to derive the usually much smaller DHI.

3.4. Kipp & zonen CSD3

The Kipp & Zonen CSD3 (shown in Fig. 4, right) is a sunshine duration sensor that avoids any moving parts [49,50]. Three photodiodes with custom-designed diffusers are located inside a glass cylinder. The glass cylinder is tilted away from the equator by an angle that equals the local latitude. An analogue calculation determines sunshine duration and DNI as a byproduct. DNI is derived from the signals E of the three photodiodes $D1$, $D2$, $D3$ as follows [46,51]:

$$DNI = a \cdot \left(E_{D1} - b \cdot \min(E_{D2}, E_{D3})\right), \tag{4}$$

where a is a sensitivity coefficient and b is a shading coefficient. Photodiode $D1$ receives direct irradiance and a part of the diffuse irradiance. $D2$ and $D3$ use an identical diffuser and orientation as $D1$. However, these are equipped with shades so that at least one of the two is always shaded. The photodiode $D2$ or $D3$ with the smaller signal is then assumed to measure a constant fraction $1/b$ of the diffuse irradiance received by $D1$. Accordingly, the subtraction in Eq. (4) corrects for the diffuse contribution to E_{D1} [46,51].

As CSD3 sensors can be operated in the same orientation over the whole year, it is expected that $D1$'s field of view forms a spherical sector that is at least 47° wide. The diffuse contribution to E_{D1} is only corrected in a simplistic way. Hence, increased measurement deviations are expected in the presence of increased circumsolar irradiance resulting from high turbidity or clouds near the sun disk, as in the case of MS-90.

Just like with the RSIs, the CSD3's photodiode pyranometers are sensitive in a spectral range of 400 to 1100 nm [50]. As no spectral correction is applied, the sensor's limited and nonuniform spectral range is expected to cause notable measurement errors.

Fig. 6. Images of CaptPro operated at CIEMAT's PSA and of PyranoCam in a solar power plant.

3.5. Sunto CaptPro

The Sunto CaptPro (shown in Fig. 6, left) provides GHI, GTI, DHI and DNI. Additionally, spectrally weighted GHI, GTI, DHI and DNI can be calculated mimicking the spectral response of a number of PV technologies. These parameters may be of interest for monitoring PV installations. The measurement system consists of eleven photodiodes, each of which has a red, green, blue and infrared channel. Each photodiode covers a circular field of view with a diameter of 55° (half sensitivity). The photodiodes are placed at different orientations under a glass dome. This way, a very coarsely resolved hemispherical image of the sky dome is captured. The exact algorithm for calculating GHI, DHI and DNI from the measured values of the photodiodes is not published. A rough description of the algorithm was given in [52].

In combination, the photodiodes are sensitive in a spectral range from 320 to 1000 nm. An adapted weighting of the color channels determines broadband radiation as well as the fraction of this radiation used by a specific PV technology with a given spectral response. The four-channel photodiodes may have the potential for enhanced broadband corrections, partly avoiding the spectral errors known for RSIs.

The calculation of an accurate DNI and DHI from the photodiode signals is expected to be complex. Based on [52], measured DNI corresponds to that from a pyrheliometer with an aperture having a half-angle of 7 to 8° depending on the sky conditions. Thus, shortcomings are expected in situations with increased circumsolar irradiance resulting, e.g., from high turbidity or the presence of clouds near the sun disk.

3.6. PyranoCam

The PyranoCam system (shown in Fig. 6, right) measures GHI with a pyranometer and derives DHI from sky images. An all-sky imager (ASI) measures sky radiance based on pixel intensities using a physical camera model. DHI is then calculated from sky radiance. The evaluation of the image information in combination with GHI from the pyranometer enables a series of corrections to be made, resulting in increased accuracy. Also, PyranoCam's hardware enables a radiometric self-calibration of the DHI measurement as described in [23]. Situations without direct irradiance are detected from the ASI images. PyranoCam's DHI is then compared to the pyranometer's GHI, which should equal DHI in such situations. This yields a calibration constant for PyranoCam's DHI and avoids any other radiometric calibration of the camera. A preliminary version of PyranoCam was presented and validated by Blum et al. [23]. In that study, PyranoCam's DHI measurement achieved a relative root mean square deviation (*rRMSD*) of 7 to 10% depending on the dataset.

In the present study, an enhanced version of the PyranoCam system is evaluated that employs two additional corrections. First, a situation-dependent broadband correction factor is determined as a function of the ratio of DHI values calculated from the red and blue channels, respectively. This factor is applied to the raw DHI measurement, which is calculated as the weighted sum of the DHI values from the red, green and blue channels [53]. Second, a machine-learning method [24] is used to correct the measurement further. This correction uses tabular features derived from intermediate results of PyranoCam and transformed sky images as inputs. It determines a corrected DHI measurement by a convolutional neural network encoder combined with fully connected layers. PyranoCam was developed with multiple years of measurement data from the sites Tabernas and Oldenburg. The current geometric calibration of the sky imager used by PyranoCam is implemented as a self-calibration, which uses observations of the sun and moon, avoiding a calibration in the laboratory as well as manual interferences on-site [54]. Appendix B describes PyranoCam's current measurement algorithm in more detail.

In the previous evaluations of PyranoCam [22,24,55], a high accuracy of PyranoCam was found under all tested conditions. Still, certain shortcomings of the method are expected where situations in disturbances strongly affect the image information. Those previous studies assumed regular cleaning of the measurement system as recommended for any radiometer. If the sky imager's lens is strongly soiled, the sun disk can be enlarged and surrounded by blurred dust patches in the recorded image. These effects can be mistaken by the algorithm as increased turbidity or thin clouds. Additionally, in cases of extremely high turbidity, a comparably large image area around the sun can become saturated. Under these conditions, stronger scattering of the measurement was observed by Broda [24], which was explained by the lack of image information.

4. Methods

This benchmarking study of DHI and DNI sensors aims to inform users about the measurement accuracy to be expected under the conditions at their respective site. This should help users to make a suitable choice of instrument. The methods applied for this purpose are described in the following.

4.1. Comparison of test systems at sites with distinct climates

First, the deviations of the test systems are compared at the four locations where multiple test sensors are set up (Tabernas, Oldenburg, Golden, Patras) using the datasets summarized in Table 1 and characterized further in Table 4. As shown in the table, the locations represent very different conditions and climates. Tabernas features a desert climate with typically low cloud cover. At the same time, atmospheric turbidity is sometimes very low and sometimes high. Oldenburg represents a humid, oceanic climate with a typically high cloud cover and highly variable radiation. Due to the high latitude, low sun elevations occur more frequently. Golden represents mountain conditions at high altitudes with snow in winter. Patras is located 1.8 km from the Mediterranean coast, which determines the climate at the site. Thus, the study design allows for comparing the performance of sensors of the same type in very different climate zones. The accuracies of the test systems are evaluated by common deviation metrics: relative root mean square deviation (*rRMSD*), relative mean absolute deviation (*rMAD*) and relative bias (*rbias*):

$$rRMSD = \frac{100\%}{\overline{Ref}} \sqrt{\frac{1}{N}\sum_{i=1}^{N}\left(Test_i - Ref_i\right)^2} \tag{5}$$

$$rMAD = \frac{100\%}{\overline{Ref}} \frac{1}{N}\sum_{i=1}^{N}\left|Test_i - Ref_i\right| \tag{6}$$

$$rbias = \frac{100\%}{\overline{Ref}} \frac{1}{N}\sum_{i=1}^{N} Test_i - Ref_i \tag{7}$$

Test denotes a vector of test measurements of a sensor and *Ref* a vector of corresponding reference measurements. $\overline{Ref}$ is the respective mean value of *Ref* over all N valid data points as given in Table 4. While all radiation parameters are evaluated as 1-min averages in this study, the metrics *rRMSD*, *rMAD* and *rbias* are also reported for 10-min averages of DHI and DNI, as coarser time resolutions are advantageous for some applications and some measurement errors may be suppressed by temporal averaging. In all evaluations of this study, timestamps with sun

Table 4
Meteorological conditions at the test sites. Listed mean GHI, DHI and DNI are calculated over the respective test period. The current Köppen climate was taken from Beck et al. [56].

	Latitude	Mean GHI [W/m^2]	Mean DHI [W/m^2]	Mean DNI [W/m^2]	Köppen climate	Special features
Tabernas	37.1°N	465	143	559	Cold desert	Sunny, mostly high-layer ice clouds
Oldenburg	53.2°N	270	131	269	Temperate oceanic	Cloudy, stratus dominant
Patras	38.3°N	419	140	469	Hot-summer Mediterranean	
Golden	39.7°N	426	121	544	Warm-summer humid continental	Snow in winter
Benguerir	32.2°N	524	167	543	Hot semi-arid	Very turbid
Perth	32.1°S	473	128	551	Hot-summer Mediterranean	Coastal, 8 km from Indian Ocean

elevation angles of less than 5° are discarded. A similar filtering of sun elevation angles below 5 to 10° was also applied in previous radiometer benchmarks [16–18,57].

The reference measurements used may themselves be subject to measurement errors. In particular, for the calibration constants of the reference measurements, standard uncertainties on the order of 1 to 2% are expected [36]. In order to exclude an influence of the calibration of the reference radiometers on the evaluation as far as possible, all test systems at a location were calibrated against the respective reference radiometers for the sensor comparison (Section 5.1) and the study on the influences of atmospheric and astronomic parameters (Section 5.3). Only for the validation of PyranoCam at six different sites (Section 5.2) was no calibration using the reference radiometers of DHI and DNI performed.

4.2. Validation of RSI and PyranoCam without on-site calibration

PyranoCam is tested at six sites on four continents (see Table 4). This evaluation includes the additional sites Benguerir and Perth. Benguerir frequently features sand-storm conditions. Perth, located on the coast of the Indian Ocean, is expected to exhibit typical coastal cloud conditions. At the four sites introduced in Section 4.1, an RSI is evaluated in comparison. Note that previous experimental studies of PyranoCam [22–24,55] used preliminary versions of the method and that the dataset used in this work has not been evaluated in other studies yet. As for the sensor comparison, standard deviation metrics are evaluated. However, in this case, the test systems are not calibrated on-site using reference DNI or DHI. PyranoCam's self-calibration is applied by default. This procedure is part of the PyranoCam method and relies only on the system's own hardware (see Section 3.6).

Accordingly, in this evaluation, RSI is calibrated on-site using only GHI from the collocated thermopile pyranometer. This procedure is expected to be practically feasible as in many solar energy projects a thermopile pyranometer for GHI is available anyway, e.g., if IEC 61,724–1 Class A is met. Correction functions described in Section 3.2 are still applied to each RSI, however with parameters determined only using GHI or reference measurements of DNI and DHI from different sites. At sites Tabernas and Oldenburg, a method developed by CSP Services GmbH is used for the calibration and correction of the measurements. This method refines the one by Lezaca et al. [58]. Dynamically for each timestamp, the last 72 hours of measurements are considered. GHI measurements from the RSI are fitted to GHI from the thermopile pyranometer thus determining the correction functions' parameters. The fit parameters are then applied to correct GHI, DNI and DHI readings from the RSI sensor.

The correction method of CSP Services GmbH requires the raw measurements from the respective RSI or RSP. As raw measurements were not available from Patras and Golden, a different approach was followed for these sites. The RSIs' correction functions for DHI were used with the parameters originally determined at different sites (Patras used parameters determined in Tabernas; Golden used default parameters provided by the manufacturer Irradiance Inc.). Calibration constants for GHI were determined as described in Section 2.3 comparing each RSI's GHI to the respective reference GHI. This calibration constant was then applied to both GHI and DHI. As in this evaluation (results in Section 5.2) no calibration based on reference DNI and DHI is performed, the methods' transferability between sites and climates is evaluated in the typical use case without reference data available on-site.

4.3. Influence of atmospheric and astronomical parameters

In the last part of the evaluation, the influences of atmospheric and astronomical parameters on the measurements of each test system are tested using data from Tabernas. Solar elevation and azimuth angles are calculated based solely on geographic coordinates and time. The month of the year is also evaluated as a possible influence. Linke turbidity is determined from measured time series of reference DNI [59,60] for each data point. Additionally, a moving hourly average of the clear-sky index of DNI is derived [61].

Circumsolar irradiance, CSI, from the sky area with a sun distance angle of 2.5 to 5° is determined from the measurements of two shaded pyranometers tracking the sun, as described in Section 2.2. The contribution of the circumsolar irradiance to DNI is calculated as CSI/DNI. The horizontal circumsolar irradiance, CSHI, is calculated based on the sun elevation angle, α:

$$CSHI = CSI \ \sin(\alpha) \tag{8}$$

From the measured spectra of DNI, DHI and GHI described in Section 2.2, the effective wavelength of DNI, DHI and GHI is calculated according to Nofuentes et al. [62], indicating the center of mass of the respective spectrum:

$$\lambda_{eff} = \frac{\int_{280\text{nm}}^{4000\text{nm}} \lambda E(\lambda) d\lambda}{\int_{280\text{nm}}^{4000\text{nm}} E(\lambda) d\lambda} \tag{9}$$

Potential influences are then evaluated as follows. First, the Spearman rank correlation coefficient (ρ) indicates the strength of the relationship between a possible influence and the respective measurement. This coefficient is not limited to linear relationships. It indicates how well the relationship between two variables can be described by a monotonic function. The relationship between the strongest identified influence and the respective measurement is visualized using a box-whisker diagram. While not shown in this publication, the relationships between all possible influences and measurements were also investigated visually using scatter-density plots. This evaluation confirmed the plausibility of the relationships indicated by ρ.

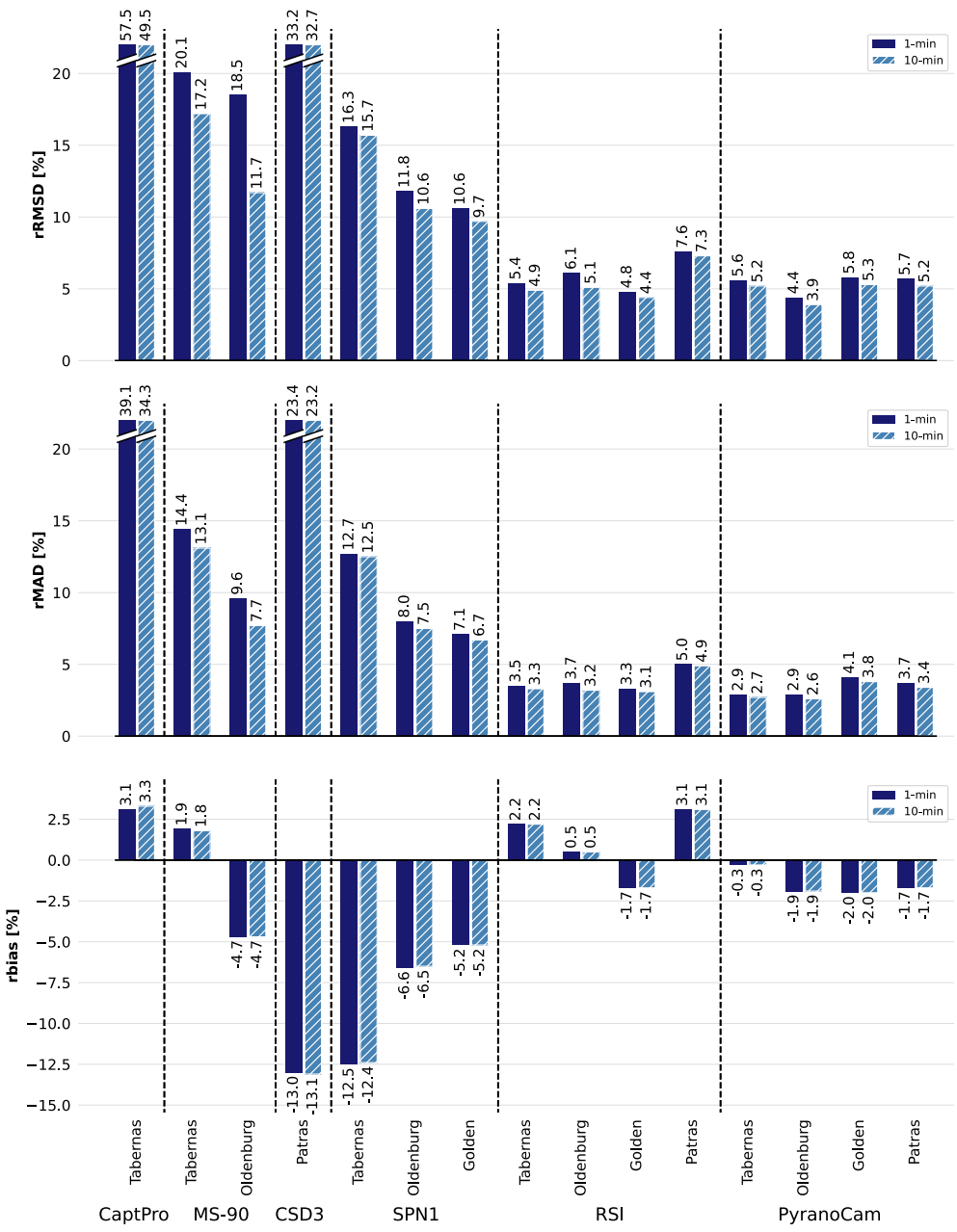

Fig. 7. Error metrics of CaptPro, MS-90, CSD3, SPN1, RSI and PyranoCam measurement systems for 1-min- (solid) and 10-min-average DHI (dashed) at the sites Tabernas, Oldenburg, Golden and Patras (where available). Note that CaptPro failed four months into the benchmark, leading to a limited and different dataset for this sensor.

5. Results

In the following, the experimental data described in Section 2 are evaluated using the methods introduced in Section 4. First, the tested sensors' accuracies are compared in Section 5.1. Then, RSI and PyranoCam are tested without on-site calibration at up to six sites in Section 5.2. Lastly, influences on the deviations of each sensor are investigated in Section 5.3.

5.1. Comparison of test systems at sites with distinct climates

The measurement systems CaptPro, MS-90, CSD3, SPN1, RSI and PyranoCam were tested at one or more of the sites Tabernas, Oldenburg, Golden and Patras. In this section, the sensor comparison is shown for DHI first and then for DNI.

5.1.1. DHI

Fig. 7 comparesthe relative deviations of all sensors' DHI measurements at the respective sites as far as they were available. At 1-min resolution, CaptPro is the least accurate sensor, with an *rRMSD* of 58%, followed by CSD3 with an *rRMSD* of 33%. Also measured by *rMAD*, both sensors' accuracies are very low, with 39% (CaptPro) and 23% (CSD3). The DIRINT decomposition model implemented in pvlib-python [15,63], based on a thermopile pyranometer for GHI and measurements of relative humidity and air temperature was evaluated in comparison to these sensors. DIRINT's *rMADs* were lower than the ones of both sensors. DIRINT's *rRMSD* was smaller than the one of CaptPro and only 2.5% points greater than the one of CSD3. Due to the calibration on-site, CaptPro's *rbias* is moderate (3.1%), whereas CSD3's *rbias* is still very large (-13%). For CaptPro, a measurement period of only four months

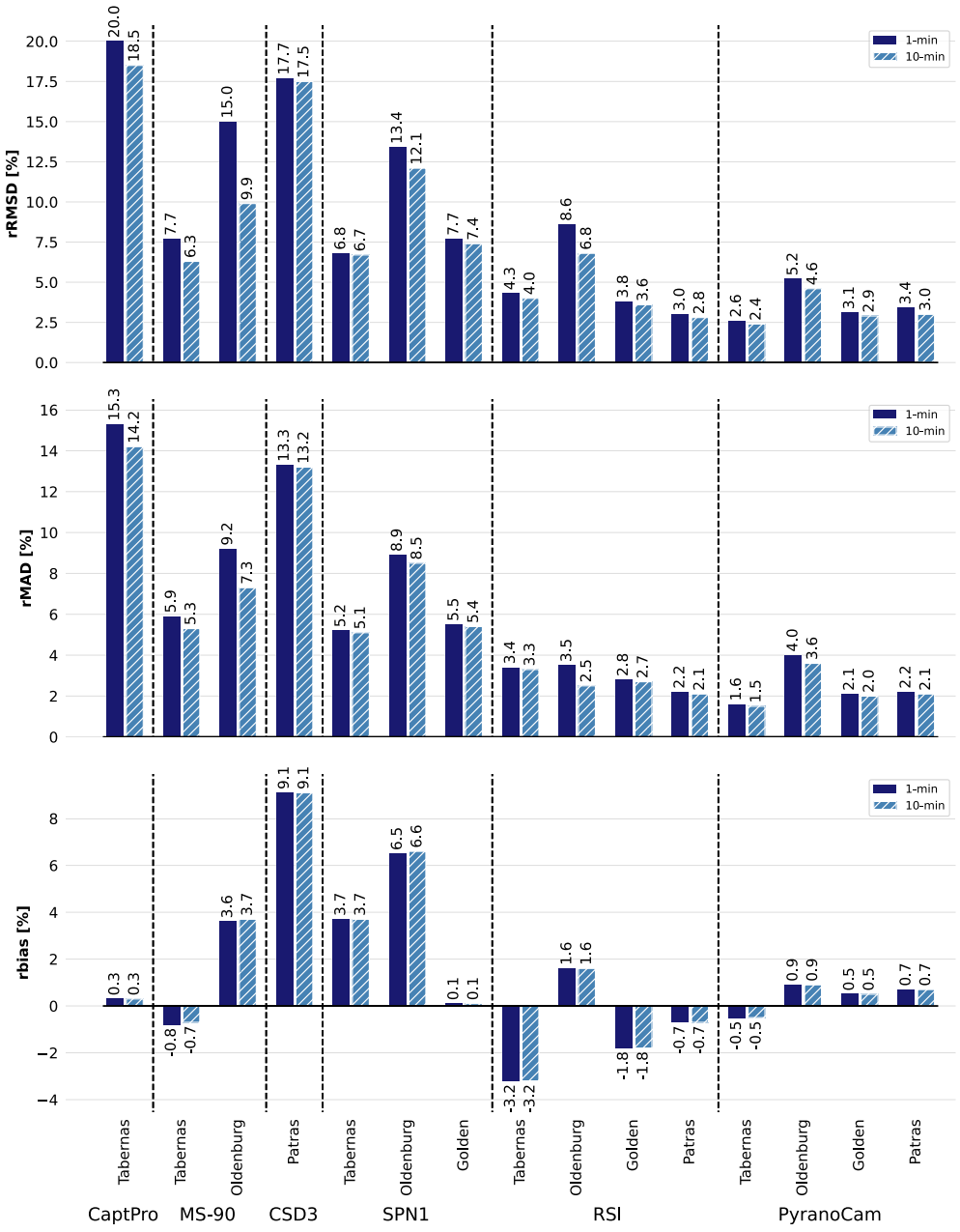

Fig. 8. Error metrics of CaptPro, MS-90, CSD3, SPN1, RSI and PyranoCam measurement systems for 1-min (solid) and 10-min average DNI (dashed) at the sites Tabernas, Oldenburg, Golden and Patras (where available).

was available. However, it is not expected that the sensor would perform better over an annual period as the remaining sensors' performances only changed moderately between the first four months and the annual period (see Appendix C). Overall, the deviations of CaptPro and CSD3 are intolerably large for DHI.

For the remaining sensors, a tendency can be seen that is similar at all sites. MS-90 has the largest *rRMSD* (18.5 to 20.1%), followed by SPN1 (10.6 to 16.3%), RSI (4.8 to 7.6%) and PyranoCam (4.4 to 5.8%). In terms of *rMAD* and *rbias*, a similar tendency is found. MS-90's *rbias* (−4.7 to 1.9%) has a smaller magnitude than SPN1's (−12.5 to −5.2%). The *rbias* of RSI (−1.7 to 3.1%) and PyranoCam (−2.0 to −0.3%) is moderate at all sites. Considering that each sensor was calibrated at the respective site, the large systematic deviations of MS-90 and in particular SPN1 are striking.

In the evaluation of 10-min averages (Fig. 7, dashed bars), small changes are found compared to the 1-min averages discussed so far. Only for MS-90, *rRMSD* and *rMAD* decrease notably at site Oldenburg, from 18.5 to 11.7% and from 9.6 to 7.7%, respectively. As MS-90 measures DNI and calculates DHI, this effect is discussed in the following section.

5.1.2. DNI

In analogy to the previous evaluation of DHI, Fig. 8 compares the relative deviations received from all sensors in terms of DNI at the respective sites. CaptPro and CSD3 are the least accurate sensors also for DNI, e.g., with an *rRMSD* of 20.0 and 17.7% at 1-min resolution, respectively. Similar to before for DHI, DIRINT predicts DNI with smaller *rRMSD* than CaptPro and only slightly larger *rRMSD* (19.2%) than CSD3. However, the gap between CaptPro, CSD3 and the remaining sensors is

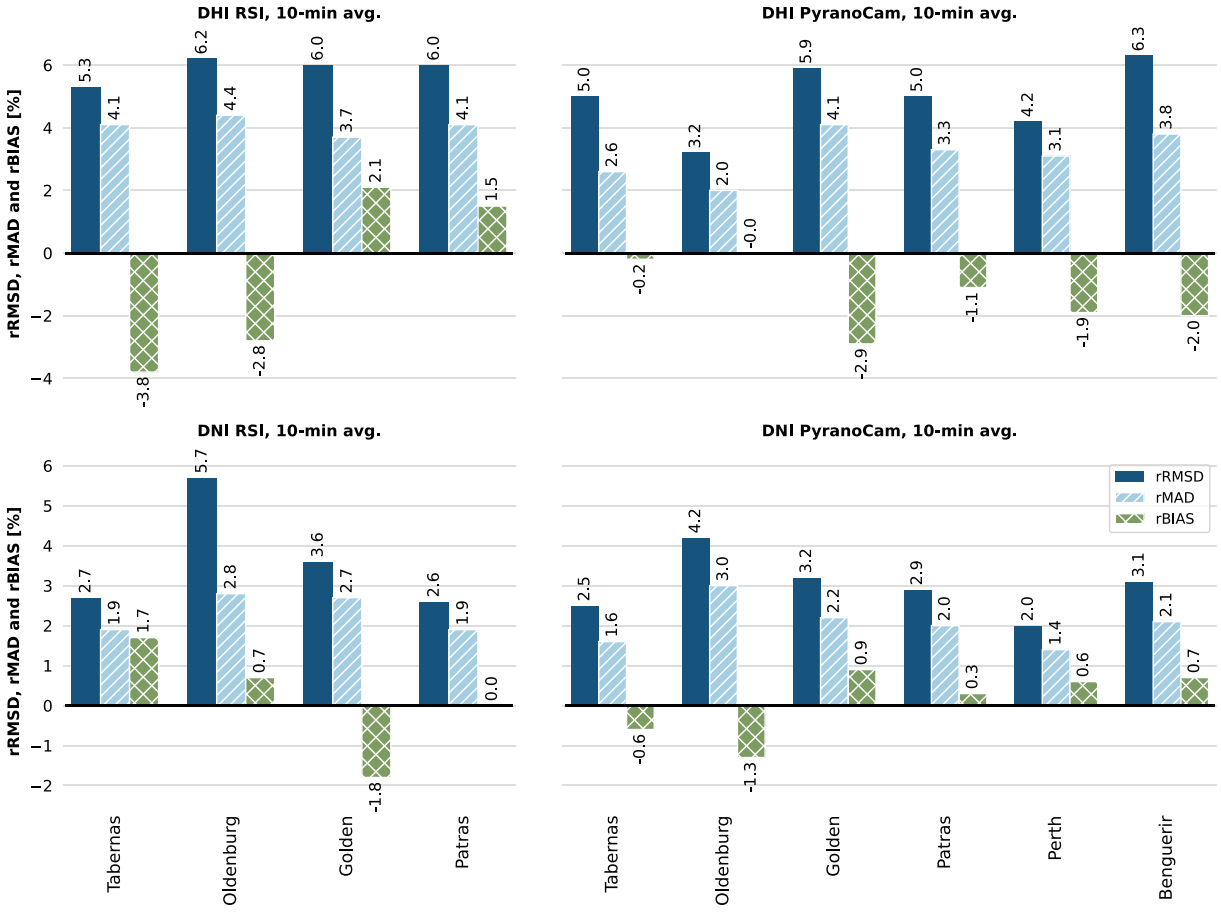

Fig. 9. Error metrics of RSI (left) and PyranoCam (right) for 10-min-average DHI (top) and DNI (bottom) at the sites Tabernas, Oldenburg, Golden, Patras, Perth and Benguerir (at the latter two only PyranoCam was operated). This evaluation represents a typical solar-energy use case and both RSI and PyranoCam are only calibrated using a collocated thermopile pyranometer.

less pronounced in the case of DNI. MS-90 and SPN1 form a class of instruments with intermediate accuracy, e.g., with *rRMSD* in the ranges 7.7 to 15.0% (MS-90) and 6.8 to 13.4% (SPN1) at 1-min resolution. In this case, depending on the site and temporal resolution, either of the two sensors can be the more accurate one. RSI and PyranoCam form a third class of instruments that consistently yield higher accuracy, e.g., with *rRMSD* at 1-min resolution in the ranges of 3.0 to 8.6% and 2.6 to 5.2%, respectively.

Looking at the systematic deviations, interestingly most sensors including CaptPro achieve a moderate *rbias* in the range −3.2 to 3.7%. Only SPN1 in Oldenburg and CSD3 have a strong *rbias* of 6.6% and 9.1% respectively.

MS-90 measures DNI and calculates DHI using GHI from a thermopile pyranometer. In Oldenburg, the sensor's *rRMSD* of both DNI and DHI decreases by 1/3 when evaluating 10- instead of 1-min averages. Such a strong reduction is only observed for MS-90. This finding is reasonable as only MS-90 measures DNI with a comparably low sampling rate of 1/(15 s). In particular in Oldenburg, DNI is much more variable than DHI at timescales below 1 min. Therefore, the RSI's even lower sampling rate of 1/(30 s) for DHI in Oldenburg is less problematic. We were able to simulate and reproduce this averaging effect accordingly for both DNI and DHI with fast-response pyranometer and pyrheliometer measurements.

5.2. Validation of RSI and PyranoCam without on-site calibration

PyranoCam was developed in Tabernas and Oldenburg and a certain overfitting of the method to the local climates and instrumentation is possible. The transferability of PyranoCam to four independent test sites is evaluated in this section. These sites were not included in the model development. In this evaluation no on-site calibration based on reference DNI and DHI is used. Only PyranoCam's self-calibration is applied. This procedure is based solely on PyranoCam's hardware and can be performed in every application of PyranoCam. Likewise the transferability of the RSI's correction functions between sites is tested as only a calibration based on GHI is carried out (see Section 4.2).

Fig. 9 summarizes the evaluation for DHI and DNI in analogy to the figures in the previous section. For conciseness, only 10-min averages are shown. Also in this evaluation, RSIs' error metrics are moderate. For DHI (Fig. 9, top left), an *rRMSD* of 5.3 to 6.2% is found. *rbias* has a slightly increased magnitude (−3.8 to 2.1%). For DNI (Fig. 9, bottom left), moderate *rRMSD* of 2.6 to 5.7% and *rbias* of −1.8 to 1.7% are found.

PyranoCam's error metrics for DHI (Fig. 9, top right) increase to some extent at the independent test sites (Golden, Patras, Perth, Benguerir) with an *rRMSD* of 4.2 to 6.3% compared to the development sites (Tabernas and Oldenburg) with an *rRMSD* of 3.2 to 5%. *rbias* remains moderate at all independent test sites (−2.9 to −1.1%). In terms of DNI (Fig. 9, bottom right), PyranoCam's accuracy at the unknown sites matches very well with the one found in Tabernas and Oldenburg. *rbias* has a magnitude of 1.3% and less at all sites. *rMAD* and *rRMSD* are in the ranges found in Tabernas and Oldenburg (*rMAD*: 1.6 to 3.0%, *rRMSD*: 2.5 to 4.2%).

Overall, RSI and PyranoCam consistently achieved high accuracy at all test sites. The sites and datasets represented different conditions regarding turbidity, cloud cover, cloud types and sun elevations.

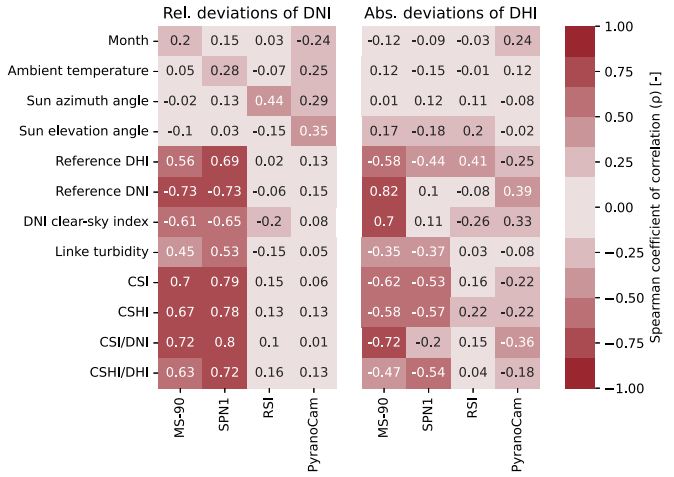

Fig. 10. Spearman coefficient of correlation ρ between atmospheric/astronomical parameters and the deviations of each sensor (left: relative deviations of DNI, right: absolute deviations of DHI).

Also in this evaluation without an on-site calibration of DHI and DNI, PyranoCam is competitive with RSI. In the case of DNI, a certain advantage of PyranoCam over RSI is evident.

5.3. Influence of atmospheric and astronomical parameters

In Tabernas, an extended measurement setup is used to identify influences on the accuracy of each sensor and to indicate their magnitude. This allows users to get a more accurate picture of the deviations to be expected in their application. Month of the year, Linke turbidity, solar elevation and azimuth angles, the hourly mean value of the clear sky index of DNI and circumsolar irradiance (CSI) including CSI/DNI, CSHI and CSHI/DHI are considered as potential influences and measured or calculated as described in more detail in Section 4.3.

Initially, the effective wavelength of DNI, DHI as well as GHI was also considered as a potential influence. However, the spectroradiometers were placed at a distance of 840 m from the remaining instruments. Thus, evaluations involving λ_{eff} were restricted to stable periods in which the spatial variation of the atmospheric parameters of interest was estimated to be small. As this filtering meant a strong limitation of the dataset, λ_{eff} was excluded from the further evaluations of this section. Instead the correlation between λ_{eff} and the remaining atmospheric parameters was investigated. $\lambda_{eff,DNI}$ was found to be related mainly to the sun elevation angle ($\rho = -0.5$) and only to a small extent to the remaining parameters ($|\rho| < 0.3$). On the other hand, $\lambda_{eff,DHI}$ was strongly correlated ($|\rho| > 0.8$) with parameters related to turbidity and cloudiness: reference DNI, circumsolar contribution to DNI, hourly clear-sky index of DNI and reference DHI. In particular for DHI measurements, this means that a strong correlation of a measurement deviation with one of these parameters may be related to a sensor's nonuniform spectral response if applicable.

Spearman correlation coefficient ρ provides an initial impression of the influence of the remaining parameters on the deviations of each measurement system as shown in Fig. 10. Since ρ can only describe monotonic relationships, the influences were also inspected visually via scatter-density plots, especially for the month of the year and the sun azimuth angle.

In the case of DHI, absolute deviations were evaluated and data points with a reference DHI < 10 W/m^2 were excluded. DHI in this range occurred seldom and corresponded to extremely dark situations e.g., during thunderstorms or around sunrise and sunset. In the evaluation for DNI, relative deviations are shown and only data points with a reference DNI > 100 W/m^2 were included. We consider this filtering to be useful, as an accurate DNI measurement is often only relevant in practical applications, e.g., when tracking solar collectors, if DNI exceeds a certain threshold. At the same time, small absolute deviations will lead to large relative deviations at smaller levels of the reference DNI and will thus obscure influences in the value range where DNI is actually of interest. In the following, the influences are discussed for the sensors MS-90, SPN1, RSI and PyranoCam one by one.

5.3.1. EKO MS-90

In the case of the MS-90, DNI itself is identified as the strongest influence on both the DNI and DHI measurements (see Fig. 10). For both measured variables, Fig. 11 confirms the clear influence of reference DNI. The box-whisker diagrams show mean and median values, interquartile ranges and 5th and 95th percentiles of the deviations of all data points that fall into a certain bin of reference DNI. In particular, a strong overestimation of DNI is observed at low reference DNI, e.g., with a median deviation of +18% for a reference DNI in the range 200 to 300 W/m^2. At higher reference DNI values, the relative deviation decreases and at a reference DNI of over 700 W/m^2 the values are comparatively small in the range −10 to +5%. Note that the zero crossing of the relative deviations was caused by the on-site calibration using all-sky conditions. Before this calibration, the relative deviations approached 0% on average from a reference DNI of 800 W/m^2. However, the uncalibrated measurement introduced larger deviations for the overall dataset. These results are consistent with the observations of previous studies [19,20]. Furthermore, the same trend was also found in Oldenburg but is not shown here for conciseness.

For both DNI and DHI, the circumsolar radiation has almost the same influence on the measurement deviations as the reference DNI in terms of ρ. The strong influence of the circumsolar radiation and the corresponding strong overestimation of DNI at low reference DNI can be explained by the fact that the MS-90's DNI measurement includes radiation from a larger and non-circular solid angle of the sky compared

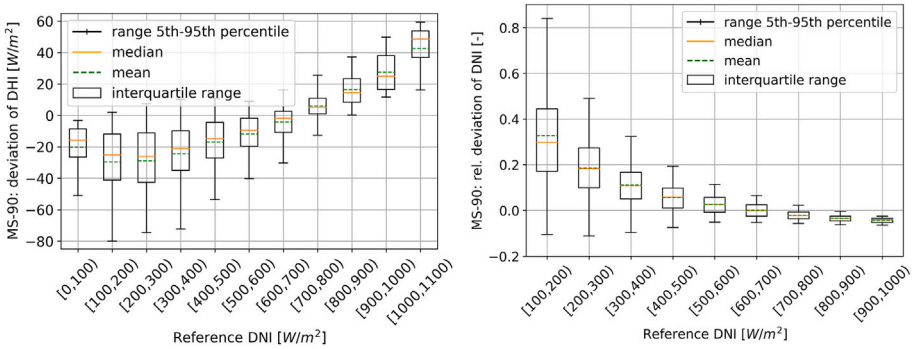

Fig. 11. Measurement deviations of the MS-90 for DHI over reference DNI (left) and relative measurement deviations of the MS-90 for DNI over reference DNI (right).

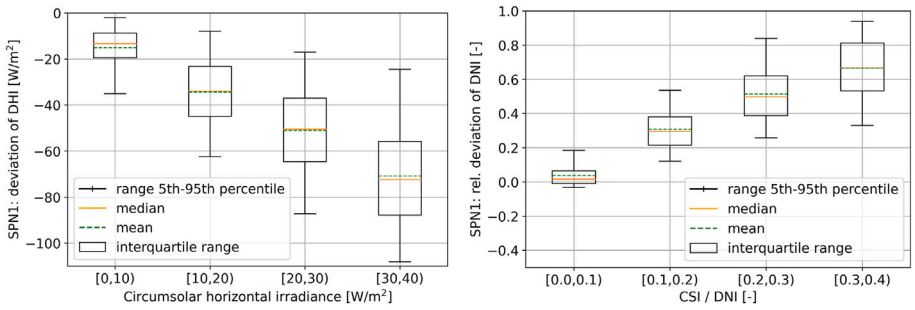

Fig. 12. Measurement deviations of SPN1 for DHI over the horizontal circumsolar radiation (left) and relative measurement deviations of SPN1 for DNI over the contribution of circumsolar radiation to DNI (right).

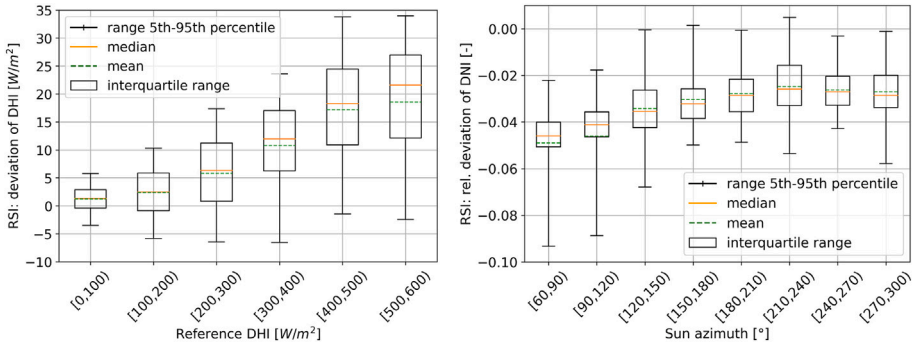

Fig. 13. Measurement deviations of the RSI for DHI over the reference DHI (left) and relative measurement deviations of the RSP for DNI over the solar azimuth angle (right).

to the measurement of a pyrheliometer. At locations with increased cloud cover or turbidity, the MS-90 is therefore expected to show increased positive deviations. Interestingly, the current evaluation, unlike that of Habte [19], suggests a rather small influence of the season on the deviations of the MS-90.

MS-90 only measures DNI. DHI is calculated using the comparably accurate GHI of a thermopile pyranometer and deviations in DHI are mainly a result of the deviations in MS-90's DNI. On the other hand, moderate relative deviations present in both DNI and GHI can be amplified when subtracting the two typically large variables GHI and direct irradiance to derive the comparably small variable DHI. This can explain the notable interquartile range of the DHI deviation which is also observed at high reference DNI.

5.3.2. Delta-t SPN1

For SPN1, circumsolar horizontal irradiance (CSHI) is identified as the greatest influence on the measurement. Fig. 12 (left) shows the influence of CSHI on SPN1's DHI measurement. With increasing CSHI, the SPN1 simultaneously introduces increasing scattering and a systematic underestimation in the DHI measurement. Interestingly, the systematic underestimation of DHI in terms of the median value corresponds to approximately twice the CSHI. This suggests that the SPN1 excludes an area around the sun disk which is significantly larger than the 10° field of view represented by the evaluated CSI measurement.

Fig. 12 (right) shows the relative deviations of SPN1 in the DNI measurement over the contribution of circumsolar irradiance to the DNI measurement CSI/DNI. In line with the results for the DHI measurement, positive deviations are visible which increase sharply with CSI/DNI. In conditions with increased circumsolar radiation, strong overestimations of DNI are observed, for example about 50% at a CSI/DNI of 0.2 to 0.3.

SPN1's attested susceptibility to circumsolar irradiance matches well with the expectations from the literature. In particular, Badosa et al. [18] measured CSHI corresponding to sun distance angles of 2.5 to 6.5° with a setup related to the one used in this study (see Section 2). Badosa et al. found that SPN1's underestimation of DHI on average equaled their measurement of CSHI. Given that the CSHI of Badosa et al. covered a solid angle which was roughly twice the one included here, the relationships found in both studies match well.

5.3.3. Rotating shadowband irradiometer (RSI)

Reference DHI and the solar azimuth angle are identified as the greatest influences on the RSI's DHI and DNI measurements, respectively (see Fig. 10). However, comparatively small deviations were found under all conditions and the correlations between all potential influences and the respective deviations are moderate. As shown in Fig. 13 (left), RSI slightly overestimates DHI as the reference DHI increases. At the same time, there is a slight underestimation of DNI. Both indicate that the calibration constant of DHI determined from a single month in summer could be slightly too large for the data of the 11-month test period and may indicate a lack of transferability of RSI's calibration constant as found in previous studies [64]. As the solar azimuth angle increases, the deviation of the DNI measurement of the RSP decreases in magnitude, from about −4.5% to about −2.5% (Fig. 13, right). This trend could indicate a slight tilt of the RSP towards the south-west.

5.3.4. PyranoCam

A moderate correlation between the reference DNI and PyranoCam's DHI as well as between the sun elevation angle and PyranoCam's DNI was found (see Fig. 10). Fig. 14 evaluates these relationships in more detail. Overall, comparably small deviations are found for PyranoCam and the systematic trends indicated e.g., by the mean values per bin of the potential influences are small compared to the measurement's moderate scattering. For the DHI measurement a slightly increased scattering of the measurement can be seen for DNI in the range 100 to 600 W/m^2. This DNI range is related to situations with increased turbidity or partial cloud cover, situations in which increased saturation of the camera

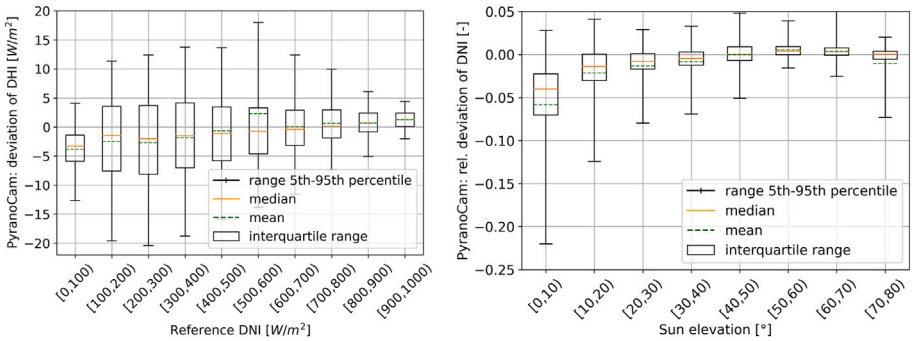

Fig. 14. Measurement deviations of PyranoCam's DHI over the reference DNI (left) and relative measurement deviations of PyranoCam's DNI over the sun elevation angle (right).

image can occur. This in turn leads to a loss of image information and can lead to increased uncertainty in the measurement. The scattering of PyranoCam's DNI measurement increases at low sun elevations. At the same time, DNI is underestimated moderately in these situations. This is plausible, as the calculation of DNI from GHI and DHI can amplify small uncertainties in GHI and DHI at low sun elevation angles.

6. Discussion

The experimental results have shown that there are significant differences in accuracy between available, practically-feasible measurement systems of DNI and DHI. Only for some of the sensors previous validations were available in the literature. The results of the current evaluation coincide well with the literature as far as available.

Sunto CaptPro exhibited very large deviations in our test (e.g., *rRMSD* of 58% for DHI; 20% for DNI). These deviations will not be acceptable for most users given that a simple pyranometer combined with a decomposition model achieved higher accuracy. The CaptPro is still a rather new instrument and very few publications on the sensor's accuracy are available. As the sensor malfunctioned four months into the comparison and could not be repaired, the data basis was limited for the current evaluation. While the exact accuracy stated for this sensor may be revised in the future based on a larger dataset potentially including further sites, we expect that the magnitude of the sensor's deviations will remain similar. Note that the instrument has a wider scope than only broadband DNI and DHI measurements. In particular, GTI for arbitrary planes, spectrally-matched to a PV technology of interest can be determined with the instrument. Such information could potentially be useful to monitor and control fixed-tilt and sun-tracked PV. This would have to be evaluated by additional measurements. Furthermore, the longevity of the sensor would need to be tested with further samples of the instrument after the observed defect.

The accuracy of Kipp & Zonen CSD3 was found to be comparatively low, similar to CaptPro. The sensor was designed as a cost-efficient sunshine duration sensor. DNI is only output as a side product. Against this background and in view of the strong simplifications used by the measurement principle regarding the spectral and angular composition of the diffuse irradiance the low performance appears reasonable. Also in the case of CSD3, the sensor's accuracy may change at a site different from Patras. Still we expect that the order of magnitude of the sensors' deviations will remain similar. As CSD3's and CaptPro's accuracy appeared insufficient for solar energy applications, they were not evaluated in more detail.

MS-90 and SPN1 showed significant deviations but may still bring a benefit for some applications given the higher accuracy compared to a basic decomposition model. The error metrics of SPN1 and MS-90 varied significantly between the test sites which indicates a certain dependence of their accuracy on the atmospheric conditions in a dataset. Note that all measurement systems were calibrated at the respective site for the comparison of the different sensors. Larger deviations are expected if the calibration errors of the reference pyranometer are not excluded in this way. The accuracies of the test systems are also expected to deteriorate if they are used in different atmospheric conditions after calibration, e.g., at a different site. On-site calibration resulted in a significant increase in accuracy for both MS-90 and SPN1.

In line with previous studies [19,20], MS-90 overestimated DNI before a relative calibration on site. As expected, this overestimation was strong at low reference DNI and decreased monotonically, approaching zero at a reference DNI of 1000 W/m^2. After the calibration on site, the bias was removed for the larger part and *rRMSD* decreased accordingly. MS-90 was only evaluated at sites Tabernas and Oldenburg. The sensor's accuracy may change at another test site. However, at both sites, DNI was the dominant influence on the sensor's deviations, as expected from the literature. The two sites feature distinct atmospheric conditions, in particular very different distributions of cloud coverage and DNI. Therefore, we expect that MS-90's accuracies found in Tabernas and Oldenburg represent the typical range of the sensor's accuracy which will be found at many sites. As an on-site calibration is usually not feasible in practice, we recommend using MS-90 only for DNI measurements at a temporal resolution of 10 min or coarser and only if mainly clear-sky conditions with low turbidity corresponding to an actual DNI > 700 W/m^2 are relevant for an application. However, these criteria represent a severe limitation. MS-90's DHI measurement was found to have low accuracy in Tabernas and Oldenburg. As mentioned in Section 5.3.1, this may be explained by the principles of error propagation. Relative errors are expected to amplify when subtracting two large signals (GHI and direct horizontal irradiance) with a moderate uncertainty to determine a comparably small signal (DHI). A similar effect was also observed for DHI calculated from GHI and CSD3's DNI.

SPN1 provided more accurate measurements at low circumsolar radiation, while the deviations in the DNI and DHI measurements increased sharply with increasing circumsolar radiation. This result was in line with the literature, in particular [18]. SPN1 could therefore be useful at locations where circumsolar radiation usually assumes low values. However, cirrus clouds, aerosols and enhancement effects associated with water clouds can all cause increased circumsolar radiation in the relevant angular range which makes this condition problematic at many sites. The comparison of SPN1 between sites confirms that its accuracy is lowest at the most turbid test site of SPN1, Tabernas. As expected besides an increased *rRMSD* a strong negative *rbias* was found. In this context, note that SPN1 was calibrated on site using its GHI measurements. The negative bias resulting from SPN1's treatment of circumsolar irradiance therefore remains after the calibration.

RSI and PyranoCam clearly stand out from the other measurement systems with the highest accuracies determined in the comparison. No influences were identified for RSI that correlated strongly with its

moderate deviations. The spectral errors reported in the literature are limited to a low level in the test dataset by the correction functions. This makes RSI a useful measurement system for many applications. Still, the literature has reported notable systematic errors of the RSI when it was calibrated at a different site than the test site [39]. We also tested RSI without an on-site calibration of DHI. In this case, errors increased slightly or decreased depending on the site.

PyranoCam provided slightly more accurate measurements than RSI. PyranoCam was tested at its development sites and four other sites in different climate zones. Only a small site-dependency was found. This appears reasonable as no atmospheric parameter was found which increased PyranoCam's deviations notably. At this point, recall that PyranoCam contains a machine-learning correction that was trained with data from Tabernas and Oldenburg over a training period well separated from, i.e., prior to, the period evaluated in this study. It is therefore indicated that PyranoCam's machine-learning correction generalizes regarding the evaluated period, site, atmospheric conditions and camera hardware / sample — as long as a Q25 or Q26 camera is used. PyranoCam's DNI, which is based on the subtraction of GHI and DHI, appears to benefit from the use of high-quality GHI. In particular at sites with a small diffuse fraction, GHI will dominate this calculation. PyranoCam is confirmed to be a generally usable measurement system requiring only a self-calibration based on the measurements of its GHI pyranometer. As an additional advantage, PyranoCam's hardware can be used to provide further parameters such as GTI in arbitrary planes, cloud cover and irradiance forecasts. At the time of writing, PyranoCam is being operated by multiple independent research facilities. Upcoming validation studies are expected to cross-check the findings of this study.

In particular for MS-90 and SPN1, the evaluation of potential atmospheric and astronomical influences on the accuracy of the test instruments provided insights into the sensors' shortcomings which may partly be avoided by further corrections. For MS-90, a simple correction based on measured DNI could strongly reduce the sensor's systematic deviations. For SPN1, an estimation of circumsolar irradiance could increase the instrument's accuracy for DHI. Badosa et al. [18] suggested multiple potential corrections in this regard. A diffuse ratio calculated from SPN1's DHI and GHI and SPN1's raw pyranometer signals could be evaluated as indicators for such a correction. Additionally, SPN1's DHI could be scaled by a constant value of 1.05. In the current tests, this would have notably reduced SPN1's *rbias* to −0.2% in Golden, −1.6% in Oldenburg and from −12.5% to −7.4% in Tabernas. We would suggest that this simple correction if not a more sophisticated one should always be applied to SPN1's measurements.

Note also that the high-end reference radiometer measurements used in this study are subject to uncertainty. Sengupta et al. [36] state 1% and 2% as calibration uncertainties of a pyrheliometer and of a diffusometer (shaded pyranometer), respectively. For the sensor comparison, these uncertainties were excluded for the most part by the on-site calibration. At the same time, it is likely that the on-site calibration has suppressed a part of the instruments' site dependent biases. On the other hand, PyranoCam's moderate systematic deviations found in the comparison between sites are only partly significant and can be influenced by the reference radiometers' uncertainties as in this case no on-site calibration of DNI and DHI was used. In a future study, uncalibrated performance should be investigated also for SPN1 and MS-90. Additionally an uncertainty budget should be specified for each sensor which combines reference uncertainty, calibration uncertainty and sampling variability.

The current evaluation focused on DNI and DHI. The uncertainty in GHI, DNI and DHI measurements impacts the uncertainty of downstream evaluations such as PV performance assessments [65] and the economic analyses of planned PV projects based on solar resource assessments [66]. In PV applications, GHI, DNI and DHI are often used as intermediate parameters only and plane-of-array irradiance (POA) is the main parameter of interest. The current evaluation should therefore be repeated for POA. Some errors e.g., those related to circumsolar irradiance may partly cancel out in the transposition process. PyranoCam and in principle also CaptPro can directly determine global and diffuse irradiance in inclined planes.

Table 5
Summary of each sensor type's relative RMSD and of the respective number of test sites evaluated. Ranges are given if multiple test sites were evaluated.

Sensor	Test sites	DNI	DHI
CaptPro	1	20.0	57.5%
CSD-3	1	17.7%	33.2%
MS-90	2	7.7 to 15.0%	18.5 to 20.1%
SPN1	3	6.8 to 13.4%	10.6 to 16.3%
RSI	4	3.0 to 8.6%	4.8 to 7.6%
PyranoCam	6	2.6 to 5.2%	4.4 to 5.8%

7. Conclusion

Measurement deviations of radiometer systems for direct and diffuse irradiance, which are relevant for solar applications, were compared at different sites worldwide. Table 5 exemplarily summarizes the sensors' rRMSDs at 1-min resolution. Rotating shadowband irradiometers (abbr. RSI; CSP Services Twin RSI, Reichert RSP 4G, Irradiance RSP v2) and PyranoCam exhibit similar error metrics and are the most accurate systems in the test. Delta-T SPN1 and EKO MS-90 but especially Kipp & Zonen CSD3 and Sunto CaptPro show significant deviations. Sensors with very low accuracy were only evaluated at a single site. The most accurate sensors, PyranoCam and RSI, were tested at the largest number of sites.

Our rather unique measurement setup made it possible to relate the deviations of the individual sensors to the actual physical causes, which were stated more qualitatively in previous studies. It was shown that the deviations of SPN1's DHI and DNI measurements increase sharply in situations with high circumsolar irradiance. MS-90's DNI measurement was influenced strongly by DNI itself. In most systems (Delta-T SPN1, CaptPro, CSD3), increased measurement errors were related to the influence of circumsolar irradiance and these instruments' apertures were in general not well defined and effectively larger than the ones assumed by ISO9060:2018 Class A pyrheliometers.

The use of SPN1 and MS-90 will be problematic at locations with high atmospheric turbidity or increased cloud cover. For the RSI and PyranoCam measuring systems, comparatively small deviations were detected under all atmospheric conditions and only moderate influences on the measurements were identified indicating a general applicability of these instruments. Still, note that a limited transferability of RSI's calibration constants was found in prior studies. Additionally, PyranoCam's high accuracy needs to be confirmed by further independent studies which are expected to be published soon.

Systematic deviations of RSI, SPN1, MS-90, CaptPro and CSD3 were to some extent suppressed by a calibration on-site. Larger deviations will occur if the instruments are transferred between sites without adjustment of the calibration constants. The calibration of the test systems may depend on the site and the conditions during calibration. Due to their spectral sensitivity, this mainly affects the photodiode-based instruments RSI, CSD3 and CaptPro and, due to the dependence on circumsolar radiation, MS-90 and SPN1.

For RSI and PyranoCam, transferability between sites without recalibration was evaluated and confirmed. PyranoCam was tested at six sites in total without an on-site calibration of DNI and DHI. The accuracy found at the development sites Tabernas and Oldenburg was confirmed. Error metrics for DNI did not increase at the four independent test sites. At the independent test sites, for DHI, a moderate *rbias* of −2.9 to −1.1% was found and *rRMSD* increased moderately from 3.2 to 5% to 4.2 to 6.3% (at 10-min resolution). The moderate *rbias* of DHI can partly be explained by the uncertainty of the reference data of DHI used in the development and validation of PyranoCam. A further improvement of

PyranoCam in this regard would require including very high-quality and even more extensive amounts of reference data of DHI in PyranoCam's further development.

Overall, this study found that with RSI and PyranoCam practically-feasible and accurate DNI and DHI sensors are available. For the less accurate sensors MS-90 and SPN1, correction functions have been discussed that can partly mitigate the sensors' systematic errors. For solar energy applications, the use of RSI and PyranoCam is recommended over expensive solar trackers prone to frequent failures. While e.g. RSI is already acknowledged in relevant standards such as IEC 61,724–1 and established guidelines (in particular [36]), these standards and guidelines may be refined in the future based on the findings of this study.

CRediT authorship contribution statement

Niklas Blum: Writing – review & editing, Writing – original draft, Visualization, Validation, Software, Resources, Project administration, Methodology, Investigation, Funding acquisition, Formal analysis, Data curation, Conceptualization. **Bijan Nouri:** Writing – review & editing, Supervision, Software, Resources. **Yann Fabel:** Writing – review & editing, Software, Resources, Data curation. **Laura Campos Guzmán:** Writing – review & editing, Software, Resources, Data curation. **Jonas Stührenberg:** Writing – review & editing, Resources, Data curation. **Andreas Kazantzidis:** Writing – review & editing, Resources. **Mounir Abraim:** Writing – review & editing, Resources, Data curation. **Martina Calais:** Writing – review & editing, Resources, Data curation. **Aron Habte:** Writing – review & editing, Resources, Data curation. **Anne Forstinger:** Writing – review & editing, Software, Data curation. **Felix Maas:** Writing – review & editing, Software, Methodology, Investigation, Data curation. **Rafal Broda:** Writing – review & editing, Visualization, Software, Investigation. **Paul Matteschk:** Writing – review & editing, Software, Investigation. **Luis F. Zarzalejo:** Writing – review & editing, Resources. **Orestis Panagopoulos:** Writing – review & editing, Resources, Data curation. **Abdellatif Ghennioui:** Writing – review & editing, Resources. **Stefan Wilbert:** Writing – review & editing, Supervision, Funding acquisition, Conceptualization.

Declaration of competing interest

The authors declare the following financial interests/personal relationships which may be considered as potential competing interests:

Coauthor Anne Forstinger is an employee of CSP Services. One of the tested correction approaches for rotating shadowband irradiometers was developed by CSP Services. CSP Services did not influence the methodology of our evaluation or the interpretation of the results obtained with their approach. PyranoCam, one of the systems tested in the benchmark, was developed by the main author. The authors have a very limited financial interest/benefit from a potential commercial success of PyranoCam. PyranoCam is licensed by a company that was not involved in this work.

Acknowledgements

We would like to thank the technical staff at all test sites. A special thanks goes to our technicians at the Tabernas site, Sergio Gonzalez Rodriguez and David Muruve Tejada for their efforts in the maintenance and cleaning of the instrumentation. This research was partly funded by the German Federal Ministry for Economic Affairs and Energy through the projects SOLREV, SOLREV-2 and ProSolNetz (grant agreement numbers 03EE1010C, 03EE1195B, 03EN6032A), based on a decision by the German Bundestag. This work was authored in part by NREL for the U.S. Department of Energy (DOE), operated under Contract No. DE-AC36-08GO28308. Funding for the NREL author was provided by the U.S. Department of Energy Office of Energy Efficiency and Renewable Energy Solar Energy Technologies Office. The views expressed in the article do not necessarily represent the views of the DOE or the U.S. Government. The U.S. Government retains and the publisher, by accepting the article for publication, acknowledges that the U.S. Government retains a nonexclusive, paid-up, irrevocable, worldwide license to publish or reproduce the published form of this work, or allow others to do so, for U.S. Government purposes.

Appendix A. Measurement of circumsolar irradiance

In Tabernas, a special setup was developed to measure circumsolar irradiance. The setup consists of two shaded and tracked CMP21 pyranometers in a sun-normal plane. The circular shades were designed to obscure sun distance angles up to 2.5° and 5° respectively. This means the pyranometers measure diffuse normal irradiance (DiffNI) corresponding to opening half-angles of 2.5° and 5°. The pyranometers were placed in a sun-normal plane instead of a more straight-forward horizontal plane to maintain a constant shading geometry at all sun elevation angles (see [32]). The two pyranometers' measurements were subtracted to yield the circumsolar irradiance from sun distance angles between 2.5° and 5°.

A.1. Design of the shading geometry

Shade diameters (R) and distances between shades and pyranometer sensor planes (L) were calculated to realize DiffNI measurements that mimic the shading geometry of Kipp & Zonen pyrheliometers as described by Major [32]. The shading geometry of these instruments is characterized by:

- Opening half-angle: $z_0 = arctan(R/L) = 2.50°$,
- Slope angle: $z_s = arctan((R-r)/L) = 1°$,
- Limit angle: $z_l = arctan((R+r)/L) = 4°$.

The radius of the pyranometer/pyrheliometer's circular receiver surface r is defined by construction and equals 10.4 mm in the case of a Kipp & Zonen CMP21. The characteristics stated above are commonly met by modern standard pyrheliometers, e.g., those of Kipp & Zonen, Hukseflux and EKO Instruments [68–70].

The 2.5°-DiffNI measurement was designed to provide a measurement complementary to that of a CHP1 pyrheliometer, i.e., to measure the difference between global normal irradiance and DNI. As a basic requirement, the corresponding shade needed to have a radius R larger than that of the pyranometer's glass dome (radius 25 mm) to exclude potential interference from reflections and refractions in the glass dome with the measurement [32]. R = 30 mm was chosen, to leave a generous tolerance for imperfections in the manufacturing and setup of the shade. By selecting L = 687 mm, a shading geometry similar to that of a CHP1 was achieved:

- Opening half-angle = 2.50°
- Slope angle = 1.63°
- Limit angle = 3.37°

The second DiffNI measurement was designed to have an opening half-angle of 5°, which is expected to correspond approximately with the of an SPN1. For practical reasons, only that shade's radius R was increased compared to the 2.5°-DiffNI measurement, whereas L and naturally r remained constant. This yielded a shading geometry characterized by the following parameters:

- Opening half-angle = 4.99°
- Slope angle = 4.13°
- Limit angle = 5.85°

To give an additional comparison, a typical diffusometer using a CMP21 (L = 577 mm, R = 25.4 mm, r = 10.4 mm), has the following shading geometry at the special case when the sun is located in the zenith (zenith angle 0°):

- Opening half-angle = 2.52°
- Slope angle = 1.49°

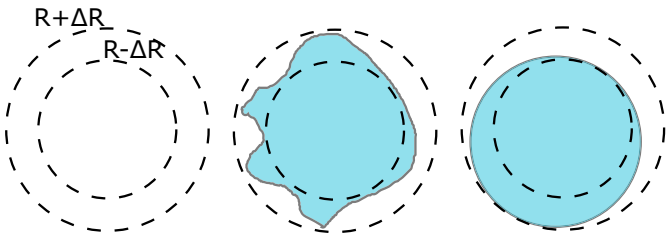

Fig. A.1. Schematic interpretation of uncertainties in the manufacturing and mounting process of the circumsolar irradiance measurement's shades which are lumped into ΔR.

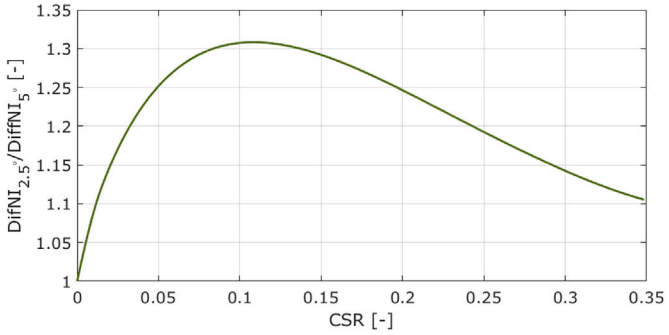

Fig. A.2. Expected ratio of the two DiffNI signals as a function of CSR based on modeled sunshapes. Already from CSR = 0.0067, the ratio of both signals exceeds 1.06 and the measurement signal is expected to be significant compared to potential measurement errors. Note that this study uses a specific definition of CSR.

- Limit angle = 3.55°

In summary, the measurement of circumsolar irradiance was designed to represent sun distance angles between 2.5° and 5° accurately. As indicated by the difference between the limit and slope angle, the measurement's penumbra function (sensitivity) features a sharper transition at the field of view's limits compared to common pyrheliometers but is very similar to a CMP21 diffusometer at a sun zenith angle of 0°.

A.2. Influence of manufacturing errors

It was estimated that the shades could be produced and positioned with an error ΔR where $|\Delta R| < 3$ mm. This error may be interpreted as shown in Fig. A.1. Furthermore, it was assumed that the distance between the shade and pyranometer sensor plane can be set with an error ΔL where $|\Delta L| < 5$ mm. Inserting $R \pm \Delta R$ and $L \pm \Delta L$ corresponding to the largest expected errors into the previous calculation, the effect of these errors on the shading geometry was estimated. For both shades, the opening half-angle, slope and limit angle were found to change by less than 0.3° in the worst cases if the tolerances are met.

A.3. Expected signal strength

To estimate signal strength, the ratio $DiffNI_{2.5°}/DiffNI_{5°}$ was modeled as a function of the circumsolar ratio CSR.

Radiance profiles in the proximity of the sun disk (sunshapes) were calculated according to Buie et al. [71] as a function of CSR. CSR is defined as $CSI/(DNI + CSI)$, with the circumsolar irradiance CSI. In the present study, circumsolar irradiance is defined as $CSI = DNI_{5°} - DNI_{2.5°}$. While Buie's definition uses a different range of sun distance angles, the following descriptions adhere to our definition.

With the shading geometries from Appendix A.1, the sums of direct and circumsolar irradiance blocked by the 2.5° and 5° shades ($DNI_{2.5°}$, $DNI_{5°}$) were calculated from the radiance profiles.

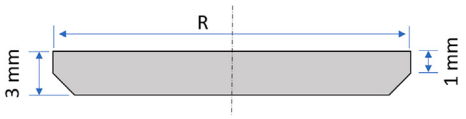

Fig. A.3. Drawing of the shades' cross-section. The shades are axially symmetrical disks with radius R. The lower circular edge is slanted to reduce the shades' thickness which affects the shading geometry.

Diffuse irradiance excluding circumsolar radiation ($DiffNI_{5°}$) is expected to increase with the circumsolar ratio as follows:

$$DiffNI_{5°} = DiffNI_{5°,CSR=0} \cdot (1 + CSR/2) \quad \text{(A.1)}$$

The equation is a very rough approximation based on an experimental evaluation at the same site (Tabernas) [72]. Scattering of direct irradiance increases with CSR and causes DHI to increase. At the same time, more radiation is reflected into space which justifies the division by two. This allows to calculate $DiffNI_{2.5°}$:

$$DiffNI_{2.5°} = DiffNI_{5°} + (DNI_{5°} - DNI_{2.5°}) \quad \text{(A.2)}$$

The resulting ratio $DiffNI_{5°}/DiffNI_{2.5°}$ as a function of CSR is visualized in Fig. A.2. From a circumsolar ratio (CSR) of around 0.0067, the ratio of the DiffNI signals exceeds 1.06. From this value onward, the measurement signal is expected to be significant compared to the errors in the measurement.

A.4. Manufacturing of the structure

The shades were manufactured on a lathe machine from an aluminum cylinder. Fig. A.3 provides an overview of their geometrical properties. The shades have the form of disks with a thickness of 3 mm and the above-mentioned radii. The circular edges on the shades' bottom sides were chamfered so that for the optical calculations the shades' thickness can be set to 1 mm and therefore be neglected. An increased thickness of the shades would influence the shading geometry and related errors discussed above. The shades are carried by an aluminum profile with a square cross-section of 6 mm-side length. This profile in turn is mounted to 20 mm ITEM profiles which are clamped to the Solys2 tracker's shading structure (shown in Fig. 2 top, right).

The distances between shades and pyranometers were checked after the setup and were confirmed to be well within the tolerance with actual distances in the range of 685 to 689 mm. The shades' actual radii deviated from the set values by less than 1 mm. The shades' centric position over the pyranometer domes was checked periodically. Based on that, the desired opening half-angle, limit and slope angle are expected to be met with deviations well below 0.3°.

A.5. Relative calibration

The individual CMP21 pyranometers' calibration constants have uncertainties of 1% and above. To minimize a potential influence of this uncertainty on the CSI measurement, the $DiffNI_{5°}$ measurement's pyranometer was calibrated in-situ relative to the $DiffNI_{2.5°}$ measurement's pyranometer. For the calibration, the shades were removed. Clear periods with $DNI > 500\ W/m^2$ and sun-elevation angles above 20° from eight days were included in the calibration.

Appendix B. PyranoCam algorithm description

A former version of the PyranoCam system was described by Blum et al. [23]. In the following the enhanced PyranoCam system used in this study is introduced.

PyranoCam's hardware consists of a horizontally leveled thermopile pyranometer and an all-sky imager of the model Mobotix Q25 or Q26. The pyranometer measures GHI, and the sky imager takes an all-sky

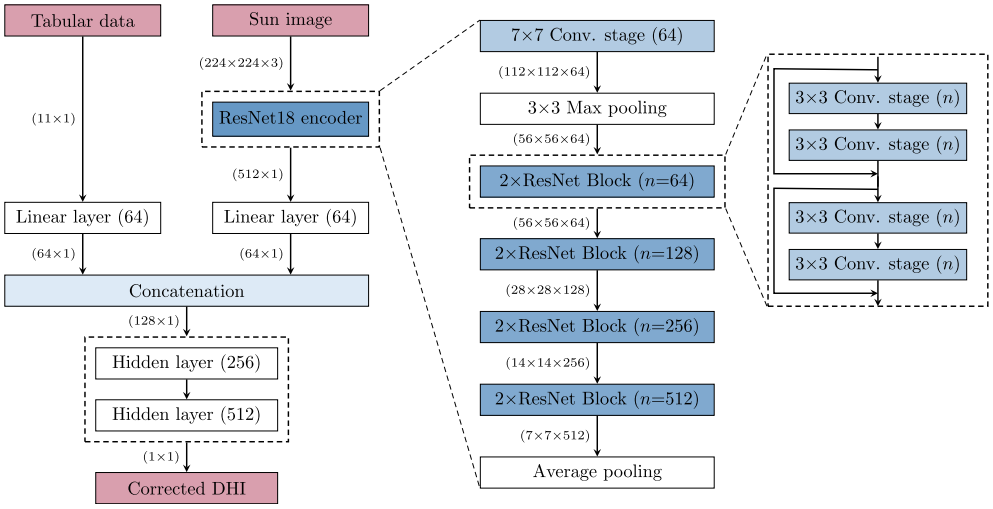

Fig. B.1. Model architecture with ResNet18 encoder, number of neurons per layer (in brackets inside the layer boxes) and output sizes of each stage (between the layers). The structure of a ResNet encoder is shown on the right. *n* indicates the number of kernels in each convolutional stage of the respective ResNet blocks. The convolutional stage applies convolution, block normalization and every Second time ReLU (rectified linear unit).

image. The camera is configured to set constant exposure settings as far as possible. Under very dark conditions a digital amplification of the pixel intensity is applied. Sky radiance is measured from the sky image's pixel intensities using a physical camera model. DHI is then calculated from sky radiance. Subsequently a number of corrections are applied.

PyranoCam was enhanced over the system from [23] by a dynamic broadband and a machine-learning-based correction. The development of PyranoCam was based exclusively on data from the sites Tabernas and Oldenburg. The development data only included periods that ended at least six months before the start dates of the periods included in the radiometer benchmark.

B.1. Dynamic broadband correction

A situation-dependent broadband correction factor (β_{bb} in [23]) was determined. This factor accounts for the variable contribution of infrared irradiance to broadband irradiance. The development of the current broadband correction was described in [53]. PyranoCam was operated in Tabernas in parallel with the WISER spectroradiometers and the reference measurements of direct and diffuse irradiance. The measurement period for this development was 12.07.2019 to 01.10.2021.

A number of potential indicators of the broadband correction factor were calculated from the measurements:

- Ratios of raw PyranoCam DHI measurements received from individual color channels (R, G, B), e.g., DHI_R/DHI_B
- Cloud cover per cloud class as defined by [73] was detected from the sky images
- Effective wavelength according to [62] was calculated from the WISER spectra
- Sun elevation angle and air mass were calculated via pvlib-python supported by local measurements of air temperature and barometric pressure
- Linke turbidity and DNI clear-sky index were determined from the DNI measurements according to [59]
- 15-min-resolution DNI variability classes according to [74] were determined from the reference DNI measurements

Raw PyranoCam DHI measurements per color channel DHI_R, DHI_G and DHI_B were calculated according to Eq. (10) in [23], setting β to [1,0,0], [0,1,0], [0,0,1] depending on the color channel (R, G, B) and using a constant β_{bb} in this intermediate step.

For model development, diffuse spectral irradiance ($E_{diff}(\lambda)$) was calculated from the WISER spectra and β_{bb} was derived as follows:

$$\beta_{bb} = \frac{\int_{280nm}^{4000nm} E_{diff}(\lambda) d\lambda}{\int_{390nm}^{700nm} E_{diff}(\lambda) d\lambda} \tag{B.1}$$

The numerator represents the diffuse broadband irradiance and the denominator represents the diffuse irradiance from the visible range alone, to which the camera is sensitive.

The ratios of DHI_R, DHI_G and DHI_B were found to be strong indicators of β_{bb}. These ratios were calculated from the PyranoCam hardware alone and were therefore easy to integrate into the PyranoCam algorithm. A continuous, piece-wise linear function with DHI_R/DHI_B (typically in the range of 0.9 to 2.0) as the argument was found to provide an accurate estimation of β_{bb} (typically in the range of 1.3 to 2.2) with an rRMSD of 4.8%.

B.2. Machine-learning-based correction

The correction factor k_{add} applied in the PyranoCam version of [23] is not applied in the current version. k_{add} accounted for disturbances related to image saturation and glare effects. Instead, such effects are corrected using a machine-learning method.

The development of this correction was described in [24]. The method uses tabular features derived from intermediate results of PyranoCam and a transformed sky image ('sun image') as inputs. A convolutional neural network (CNN) encoder extracts features from the sun image. Subsequent fully connected layers process the tabular and image features and determine a corrected DHI measurement. DNI is calculated from GHI and the corrected DHI.

The tabular features were calculated or selected from PyranoCam intermediate results which were expected to be related to PyranoCam's DHI measurement and remaining sources of errors. From 33 considered features, highly redundant features, measured by the Spearman coefficient, were rejected. Additionally, a random forest analysis was performed to test which parameters could be useful to provide an accurate estimation of DHI. Only features were retained for which an importance of 0.001 and above was indicated. In summary, the following eleven features (sorted by importance) were selected:

- PyranoCam's DHI measurement (before machine-learning correction)
- Illuminance calculated from the R channel
- Illuminance calculated from the G channel
- Illuminance calculated from the B channel
- Contribution of circumsolar irradiance including sun distance angles up to 25° to PyranoCam's DHI
- GHI from the thermopile pyranometer
- Number of saturated image pixels in the entire sky image
- Ratio of illuminances calculated from the G over R channel
- Sun elevation angle
- Ratio of illuminances calculated from the B over R channel
- PyranoCam's DNI measurement (before machine-learning correction)

Note that these features (but not the final model training) were selected before the development of the situation-dependent broadband correction. This may have influenced the feature selection to a certain extent. In particular, the importance of illuminance calculated from individual color channels is expected to have decreased.

In each timestamp, a sun image was created from the raw sky image focusing on the sky area that was expected to contain the most information on image saturation and glare effects. As the sun disk and surrounding clouds may appear distorted depending on the sun elevation, the camera's geometric calibration was used to transform the original sky image into one that mimics a camera mounted in a sun-normal plane with the sun in the image center.

The size of the square-shaped sun image was determined dynamically at every timestamp. The sun image's minimum side lengths were set to a quarter of the original sky image's smaller side length h which equaled 2048 pixels. In the presence of an increased number of saturated pixels n_{sat}, the side lengths $window_size$ were increased over the minimum value as follows:

$$window_size = \min(\{\max(\{3\sqrt{n_{sat}}, h/4\}), h\}) \tag{B.2}$$

This way even in the presence of extreme image saturation, e.g., during stand-storm conditions, a margin around the saturated sun disk was included in the sun image. The transformed sky image was cropped to a square area with side lengths $window_size$ around the image center, i.e., around the sun position. The sun image was sampled down to side lengths of 224 pixels.

Model architecture and training procedure were optimized through a parameter study, see [24]. The CNN encoder from ResNet18 [75], pretrained using self-supervised tasks, proved to be beneficial. The overall model architecture including the individual layers, neurons per layer and the number of features passed between model layers is summarized in Fig. B.1. The final supervised training of this correction included over four years of data from the sites Tabernas (01.08.2019 to 31.12.2021) and Oldenburg (01.01.2020 to 31.12.2021). This development dataset was split into a training dataset (approximately 75% of all data points) and a validation dataset (approximately 25% of all data points). Of all dates with at least one valid data point, every fourth date was assigned to the validation dataset and all remaining dates were assigned to the training dataset. These development periods ended seven months prior to the measurement periods from the sites Tabernas and Oldenburg evaluated in the present study (compare Table 1).

Appendix C. Sensor comparison restricted to periods with valid readings from CaptPro

In Section 5.1, the accuracy of CaptPro was evaluated over the dataset available from this sensor in Tabernas whereas all other sensors were evaluated over a larger dataset. Figs. C.1 and C.2 are created in analogy to Figs. 7 and 8, however in this case only Tabernas and only the period with measurements from CaptPro is evaluated for all sensors available at this site. For conciseness, only 10-min average irradiance is evaluated here. The direct comparison on an identical period confirms the difference in accuracy between CaptPro and the remaining instruments found in the evaluation of Section 5.1.

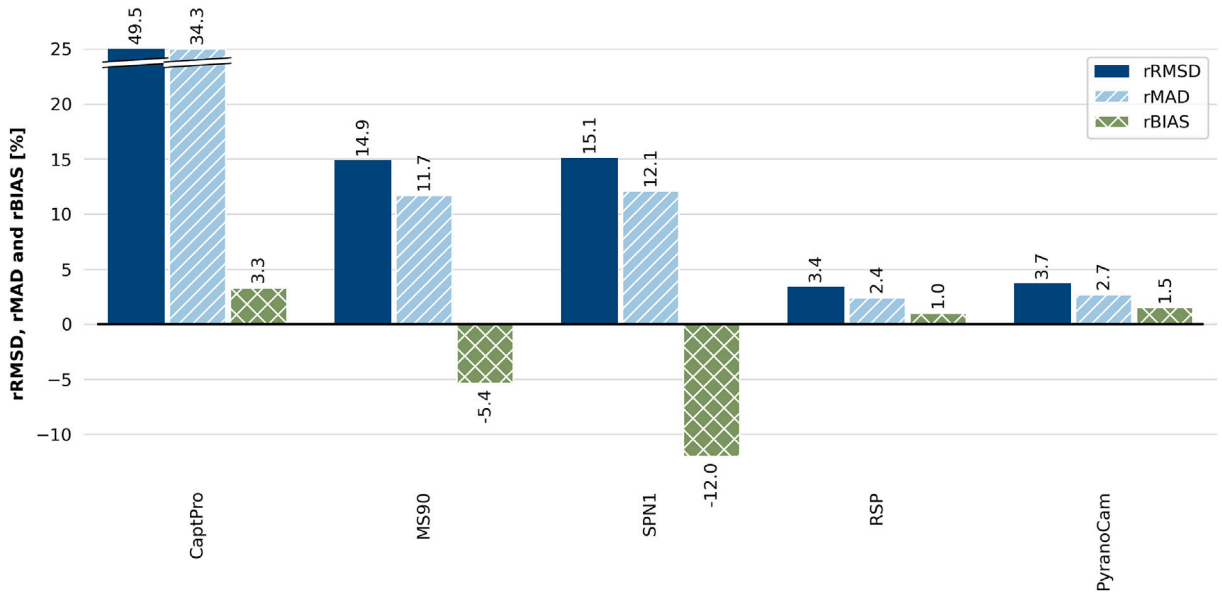

Fig. C.1. Error metrics for 10-min-average DHI in Tabernas restricted to the period with valid measurements from CaptPro.

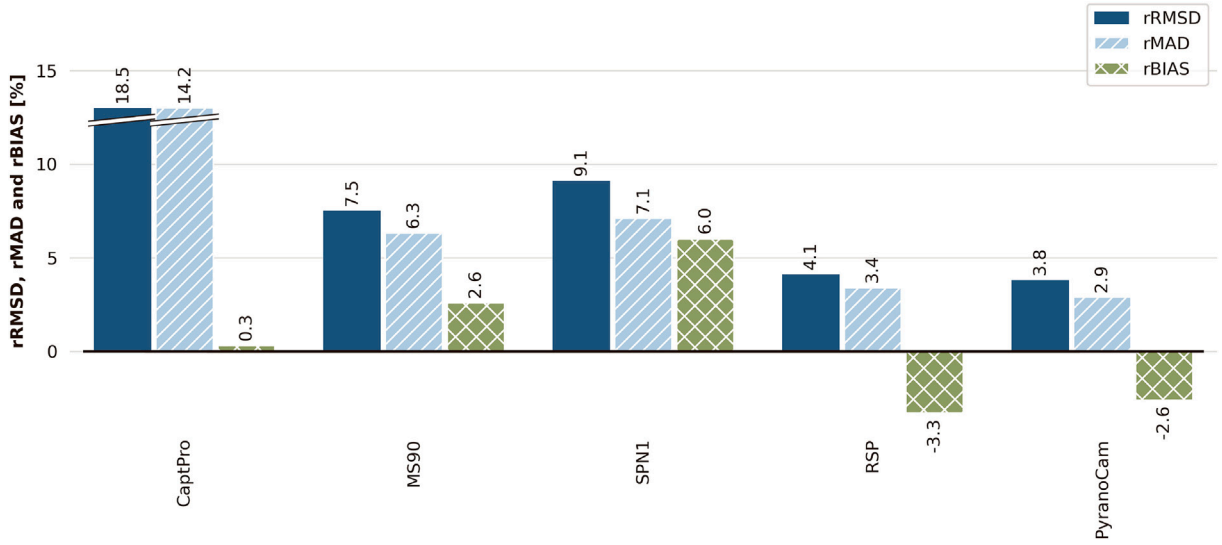

Fig. C.2. Error metrics for 10-min-average DNI in Tabernas restricted to the period with valid measurements from CaptPro.

Data availability

The measurement data used in this study are publicly available in part. Camera images and measurements of reference DNI, DHI and GHI evaluated for the Tabernas site were published by Fabel et al. [67]. All measurements taken in Golden apart from PyranoCam's DNI and DHI are publicly available and were received from NREL's web interface [25].

References

[1] International Electrotechnical Commission, Photovoltaic System Performance - Part 1: Monitoring, Standard, IEC 61724-1:2021, 2021.

[2] C.D. Rodríguez-Gallegos, H. Liu, O. Gandhi, J.P. Singh, V. Krishnamurthy, A. Kumar, J.S. Stein, S. Wang, L. Li, T. Reindl, I.M. Peters, Global techno-economic performance of bifacial and tracking photovoltaic systems, Joule 4 (7) (2020) 1514–1541, https://doi.org/10.1016/j.joule.2020.05.005

[3] E. Lorenz, P. Guthke, A. Dittmann, N. Holland, W. Herzberg, S. Karalus, B. Müller, C. Braun, W. Heydenreich, Y.-M. Saint-Drenan, High resolution measurement network of global horizontal and tilted solar irradiance in southern Germany with a new quality control scheme, Sol. Energy 231 (2022) 593–606, https://doi.org/10.1016/j.solener.2021.11.023

[4] T. Schmidt, J. Stührenberg, N. Blum, J. Lezaca, A. Hammer, S. Wilbert, B. Nouri, M. Schroedter-Homscheidt, D. Heinemann, T. Vogt, Eye2Sky – A Network of All-Sky Imager and Meteorological Measurement Stations for High Resolution Nowcasting of Solar Irradiance 34 (1), 2025, https://doi.org/10.1127/metz/2025/1245 35–55.

[5] M. Rittmann-Frank, M. Battaglia, J. Möllenkamp, M. Rommel, A. Häberle, Direct radiation measurements for the evaluation of process heat systems with concentrating solar thermal collectors, in: Proceedings of the ISES EuroSun 2016 Conference, 2016, pp. 385–394, https://doi.org/10.18086/eurosun.2016.02.13

[6] D. Lindelöf, N. Morel, A field investigation of the intermediate light switching by users, Energy Build. 38 (7) (2006) 790–801, https://doi.org/10.1016/j.enbuild.2006.03.003

[7] M. Ichinose, T. Inoue, T. Nagahama, Effect of retro-reflecting transparent window on anthropogenic urban heat balance, Energy Build. 157 (2017) 157–165, https://doi.org/10.1016/j.enbuild.2017.01.051

[8] Q. Liu, Z. Yang, W. Zhou, T. Wang, Y. Fu, X. Yue, H. Chen, Y. Tao, F. Deng, X. Lei, W. Ren, Y. Chen, Solar radiation utilization of five Upland–paddy cropping systems in low-light regions promoted by diffuse radiation of paddy season, Agric. for. Meteorol. 338 (2023) 109527, https://doi.org/10.1016/j.agrformet.2023.109527

[9] O. Urban, D. Janouš, M. Acosta, R. Czerný, I. Marková, M. Navrátil, M. Pavelka, R. Pokorný, M. Šprtová, R. Zhang, V. Špunda, J. Grace, M. V. Marek, Ecophysiological controls over the net ecosystem exchange of mountain spruce stand. Comparison of

the response in direct VS. diffuse solar radiation, Glob. Change Biol. 13 (1) (2007) 157–168, https://doi.org/10.1111/j.1365-2486.2006.01265.x
[10] M. Wild, M.Z. Hakuba, D. Folini, P. Dörig-Ott, C. Schär, S. Kato, C.N. Long, The cloud-free global energy balance and inferred cloud radiative effects: an assessment based on direct observations and climate models, Clim. Dyn. 52 (2019) 4787–4812, https://doi.org/10.1007/s00382-018-4413-y
[11] R. Hogan, M. Ahlgrimm, G. Balsamo, A. Beljaars, P. Berrisford, A. Bozzo, F.D. Giuseppe, R. Forbes, T. Haiden, S. Lang, M. Mayer, I. Polichtchouk, I. Sandu, F. Vitart, N. Wedi, Radiation in Numerical Weather Prediction, Report 816, ECMWF, Shinfield Park, Reading, RG2 9AX, England Oct 2017, https://doi.org/10.21957/2bd5dkj8x
[12] M. Gostein, A. Hoffman, B.H. King, A. Marquis, Measuring global, direct, diffuse, and ground-reflected irradiance using a reference cell array, in: 2022 IEEE 49th Photovoltaics Specialists Conference (PVSC), IEEE, 2022, pp. 0285–0290, https://doi.org/10.1109/PVSC48317.2022.9938489
[13] M. Gostein, B. Stueve, K. Passow, A. Panchula, Evaluating a model to estimate GHI, DNI, & DHI from POA irradiance, in: 2016 IEEE 43rd Photovoltaic Specialists Conference (PVSC), IEEE, 2016, pp. 0943–0946, https://doi.org/10.1109/PVSC.2016.7749749
[14] P. Ineichen, Comparison and validation of three global-to-beam irradiance models against ground measurements, Sol. Energy 82 (6) (2008) 501–512, https://doi.org/10.1016/j.solener.2007.12.006
[15] P. Ineichen, R. Perez, R. Seal, E. Maxwell, A. Zalenka, Dynamic global-to-direct irradiance conversion models, ASHRAE Trans. 98 (1) (1992) 354–369, https://archive-ouverte.unige.ch/unige:38583.
[16] L. Vuilleumier, C. Félix, F. Vignola, P. Blanc, J. Badosa, A. Kazantzidis, B. Calpini, Performance evaluation of radiation sensors for the solar energy sector, Meteorol. Z. 26 (5) (2017) 485–505, https://doi.org/10.1127/metz/2017/0836
[17] A. Habte, M. Sengupta, A. Andreas, S. Wilcox, T. Stoffel, Intercomparison of 51 radiometers for determining global horizontal irradiance and direct normal irradiance measurements, Sol. Energy 133 (2016) 372–393, https://doi.org/10.1016/j.solener.2016.03.065
[18] J. Badosa, J. Wood, P. Blanc, C.N. Long, L. Vuilleumier, D. Demengel, M. Haeffelin, Solar irradiances measured using SPN1 radiometers: uncertainties and clues for development, Atmos. Meas. Tech. 7 (2014) 4267–4283, https://doi.org/10.5194/amt-7-4267-2014
[19] A. Habte, Solar Radiometer Instrumentation Evaluation: Cooperative Research and Development Final Report, Report NREL/TP-5D00-81853; CRD-16-00619, National Renewable Energy Laboratory (NREL), Golden, CO, 2022, https://doi.org/10.2172/1841135
[20] M. Pó, K. Hoogendijk, I. Chiba, A. Akiyama, W. Beuttell, Direct normal irradiance measurements using a tracker-less sunshine duration measurement concept, in: Proceedings of the 35th European Photovoltaic Solar Energy Conference and Exhibition in Brussels, Belgium, 2018, pp. 1676–1678, https://doi.org/10.4229/35thEUPVSEC20182018-6DO.10.5
[21] M. Battaglia, J. Möllenkamp, M. Rittmann-Frank, A. Häberle, Solar irradiance measurements for the monitoring and evaluation of concentrating systems, AIP Conf. Proc. 2033 (1) (2018) 190003, https://doi.org/10.1063/1.5067188
[22] N. Blum, F. Maas, J. Stührenberg, R. Broda, P. Matteschk, M. Meinel, B. Nouri, L. Campos Guzman, A. Kazantzidis, M. Abraim, A. Ghennioui, M. Calais, A. Habte, M. Pó, L.F. Zarzalejo, S. Wilbert, A benchmark of simple diffuse and direct irradiance measurement systems, in: Proceedings of the 40th European Photovoltaic Solar Energy Conference and Exhibition in Lisbon, Portugal, 2023, https://elib.dlr.de/199101/., p. 020363001 –020363035.
[23] N. Blum, S. Wilbert, B. Nouri, J. Lezaca, D. Huckebrink, A. Kazantzidis, D. Heinemann, L.F. Zarzalejo, M.J. Jiménez, R. Pitz-Paal, Measurement of diffuse and plane of array irradiance by a combination of a pyranometer and an all-sky imager, Sol. Energy 232 (2022) 232–247, https://doi.org/10.1016/j.solener.2021.11.064
[24] R. Broda, Development of a Machine-Learning-Based Correction for Cloud-Camera-Based Solar Radiation Measurement (Thesis), RWTH Aachen, 2022, https://elib.dlr.de/189139/.
[25] A. Andreas, T. Stoffel, NREL Solar Radiation Research Laboratory (SRRL): Baseline Measurement System (BMS), NREL Report No. DA-5500-56488, 1981, https://doi.org/10.5439/1052221
[26] EKO INSTRUMENTS CO. LTD, WISER I Spectroradiometer, Report PS-EKO-MS711_712-22-01E, Tokyo, Japan Aug 2022. https://web.archive.org/web/20251007094641/https://eko-instruments.com/wp-content/uploads/2024/07/ps_wiser-i-eng-08-2022.pdf.
[27] C. Anderson, Benchmarking of Different Solar Spectra Quality Control Methods (Thesis), Queensland University of Technology, 2020, https://doi.org/10.5204/thesis.eprints.201343
[28] W. Jessen, S. Wilbert, C.A. Gueymard, J. Polo, Z. Bian, A. Driesse, A. Habte, A. Marzo, P.R. Armstrong, F. Vignola, L. Ramírez, Proposal and evaluation of subordinate standard solar irradiance spectra for applications in solar energy systems, Sol. Energy 168 (2018) 30–43, https://doi.org/10.1016/j.solener.2018.03.043
[29] C. Gueymard, SMARTS2: A Simple Model of the Atmospheric Radiative Transfer of Sunshine: Algorithms and Performance Assessment, Report FSEC-PF-270-95, Florida Solar Energy Center/ University of Central Florida, Cocoa, FL Dec 1995. https://web.archive.org/web/20260114081330/www.fsec.ucf.edu/en/publications/pdf/FSEC-PF-270-95.pdf.
[30] B.N. Holben, T.F. Eck, I.A. Slutsker, D. Tanre, J. Buis, A. Setzer, E. Vermote, J.A. Reagan, Y. Kaufman, T. Nakajima, AERONET—a federated instrument network and data archive for aerosol characterization, Remote Sens. Environ. 66 (1) (1998) 1–16, https://doi.org/10.1016/S0034-4257(98)00031-5
[31] S. Nann, C. Riordan, Solar spectral irradiance under clear and cloudy skies: measurements and a semiempirical model, J. Appl. Meteorol. Climatol. 30 (4) (1991) 447–462, https://doi.org/10.1175/1520-0450(1991)030%3C0447:SSIUCA%3E2.0.CO;2
[32] G. Major, Circumsolar Correction for Pyrheliometers and Diffusometers, Report WMO/TD-No. 635, Hungarian Meteorological Service, Budapest, Hungary Oct 1994.
[33] N. Geuder, F. Wolfertstetter, S. Wilbert, D. Schüler, R. Affolter, B. Kraas, E. Lüpfert, B. Espinar, Screening and flagging of solar irradiation and ancillary meteorological data, Energy Procedia 69 (2015) 1989–1998, https://doi.org/10.1016/j.egypro.2015.03.205
[34] J. Wood, User Manual for the Sunshine Pyranometer Type SPN1, Report, SPN1-UM-4.2, Delta-T Devices Ltd, Cambridge, United Kingdom, 2019. https://web.archive.org/web/20251007100127/https://delta-t.co.uk/wp-content/uploads/2019/06/SPN1_User_Manual_4.2.pdf.
[35] R. Perez, P. Ineichen, R. Seals, J. Michalsky, R. Stewart, Modeling daylight availability and irradiance components from direct and global irradiance, Sol. Energy 44 (5) (1990) 271–289, https://doi.org/10.1016/0038-092x(90)90055-h
[36] M. Sengupta, A. Habte, S. Wilbert, C. Gueymard, J. Remund, E. Lorenz, W.V. Sark, A.R. Jensen, Best Practices Handbook for the Collection and Use of Solar Resource Data for Solar Energy Applications, Report IEA-PVPS 16-6:2024, ISBN 978-3-907281-66-6, International Energy Agency Photovoltaic Power Systems Programme (IEA PVPS) Sep 2024, https://doi.org/10.69766/ENEH5295
[37] G. Blackburn, F. Vignola, Spectral distributions of diffuse and global irradiance for clear and cloudy periods, in: C. Fellows (Ed.), World Renewable Energy Forum, Denver, CO, 2012, pp. 4810, https://solardata.uoregon.edu/download/Papers/SpectralDistributionsofDiffuseandGlobalIrradianceforClearandCloudyPeriods.pdf.
[38] S. Wilbert, S. Kleindiek, B. Nouri, N. Geuder, A. Habte, M. Schwandt, F. Vignola, Uncertainty of rotating shadowband irradiometers and Si-pyranometers including the spectral irradiance error, AIP Conf. Proc. 1734 (1) (2016) 150009, https://doi.org/10.1063/1.4949241
[39] A. Forstinger, S. Wilbert, A. Driesse, N. Hanrieder, R. Affolter, S. Kumar, N. Goswami, N. Geuder, F. Vignola, L. Zarzalejo, A. Habte, Physically based correction of systematic errors of rotating shadowband irradiometers, Meteorol. Z. 29 (2020) 19–39, https://doi.org/10.1127/metz/2019/0972
[40] N. Geuder, M. Hanussek, J. Haller, R. Affolter, S. Wilbert, Comparison of corrections and calibration procedures for rotating shadowband irradiance sensors, in: SolarPACES 2011, Granada, Spain, 2011.
[41] F. Vignola, J. Peterson, F. Mavromatakis, S. Wilbert, A. Forstinger, M. Dooraghi, M. Sengupta, Removing biases from rotating shadowband radiometers, in: AIP Conference Proceedings, vol. 2126, AIP Publishing LLC, 2019, https://doi.org/10.1063/1.5117714, p. 190017.
[42] D.L. King, D.R. Myers, Silicon-photodiode pyranometers: operational characteristics, historical experiences, and new calibration procedures, in: Conference Record of the Twenty Sixth IEEE Photovoltaic Specialists Conference-1997, IEEE, 1997, pp. 1285–1288, https://doi.org/10.1109/PVSC.1997.654323
[43] E.C. Kern, Calibration methods for silicon photodiode pyranometers used in rotating shadowband radiometers, in: SolarPACES Conference Proceedings, Perpignan, France, 2010, pp. 21–24.
[44] D.L. King, W.E. Boyson, B.R. Hansen, Improved Accuracy for Low-Cost Solar Irradiance Sensors, Report SAND–97-3175C, Sandia National Lab.(SNL-NM), Albuquerque, NM Dec 1997, https://doi.org/10.2172/661542
[45] H. Ikeda, T. Aoshima, Y. Miyake, Development of a new sunshine-duration meter, Journal of the Meteorological Society of Japan. Ser. II 64 (6) (1986) 987–993, https://doi.org/10.2151/jmsj1965.64.6_987
[46] Y. Wang, G. Zhang, G. Sun, S. Liu, D. Xu, S. Yang, L. Wu, A review on sunshine recorders: evolution of operation principle and construction, Measurement 186 (2021) 110138, https://doi.org/10.1016/j.measurement.2021.110138
[47] EKO INSTRUMENTS CO. LTD, DNI Sensor MS-90 – Instruction Manual Version 2, Report, Tokyo, Japan 15 Jan 2019. https://web.archive.org/web/20251007085529/https://eko-instruments.com/asia/wp-content/uploads/sites/13/2024/08/ms-90-manual.pdf.
[48] R. Jayaraman, D.L. Maskell, Temporal and spatial variations of the solar radiation observed in Singapore, Energy Procedia 25 (2012) 108–117, https://doi.org/10.1016/j.egypro.2012.07.015
[49] Kipp&Zonen, CSD 3 Sunshine Duration Sensor, Report 4414365-V1201, Delft, The Netherlands, 2025. https://web.archive.org/web/20251007102924/https://www.kippzonen.com/Download/92/CSD-3-Sunshine-Duration-Sensor-Brochure.
[50] Kipp&Zonen, Instruction Sheet – CSD 3 Sunshine Duration Sensor, Report 0342321-V1810, Delft, The Netherlands, 2018. https://web.archive.org/web/20251007103148/https://www.kippzonen.com/Download/91/Instruction-Sheet-CSD3-Sunshine-Duration-Sensor.
[51] Campbell Scientific Ltd, CSD3 Sunshine Duration Sensor – User Guide, Report, Shepshed, Loughborough, UK, 2.01.07, 2002. https://web.archive.org/web/20251007093415/https://s.campbellsci.com/documents/eu/manuals/csd3%20-%20609.pdf.
[52] L. Rosa, User Instruction Manual CaptPro + All-Out Irradiation Sensor with RS485 Modbus Output, Report, Alitec, Cascina, Italy 21 Dec 2021.
[53] P. Matteschk, Physikalische Weiterentwicklung Einer Wolkenkamera-Basierten Messmethode Für Diffusstrahlung (Thesis), Technische Universität Dresden, 2024.
[54] N. Blum, P. Matteschk, Y. Fabel, B. Nouri, R. Roman, L.F. Zarzalejo, J.C. Antuña-Sánchez, S. Wilbert, Geometric calibration of all-sky cameras using sun and moon positions: a comprehensive analysis, Sol. Energy 295 (2025) 113476, https://doi.org/10.1016/j.solener.2025.113476
[55] N. Blum, F. Maas, J. Stührenberg, R. Broda, P. Matteschk, M. Meinel, B. Nouri, L. Campos Guzman, A. Kazantzidis, M. Abraim, A. Ghennioui, M. Calais, A. Habte, L.F. Zarzalejo, S. Wilbert, Bewertung von messsystemen DER direkt- und diffusstrahlung unter unterschiedlichen klimabedingungen, in: Tagungsunterlagen

39. PV-Symposium / BIPV-Forum, Conexio-PSE GmbH, Pforzheim, Germany, 2024, pp. 250–267, https://elib.dlr.de/203199/.
[56] H.E. Beck, T.R. McVicar, N. Vergopolan, A. Berg, N.J. Lutsko, A. Dufour, Z. Zeng, X. Jiang, A.I.J.M. van Dijk, D.G. Miralles, High-resolution (1 km) köppen-geiger maps for 1901–2099 based on constrained cmip6 projections, Sci. Data 10 (1) (2023) 724, https://doi.org/10.1038/s41597-023-02549-6
[57] S. Wilcox, D.R. Myers, Evaluation of Radiometers in Full-Time Use at the National Renewable Energy Laboratory Solar Radiation Research Laboratory, Report NREL/TP-550-44627, National Renewable Energy Lab. (NREL), Golden, CO Nov 2008, https://doi.org/10.2172/946331
[58] J. Lezaca, R. Meyer, D. Heinemann, Study of an extended correction algorithm for rotating shadowband irradiometers (RSI) based on simultaneous thermal GHI measurements, AIP Conf. Proc. 2033 (1) (2018), https://doi.org/10.1063/1.5067194
[59] B. Nouri, S. Wilbert, L. Segura, P. Kuhn, N. Hanrieder, A. Kazantzidis, T. Schmidt, L. Zarzalejo, P. Blanc, R. Pitz-Paal, Determination of cloud transmittance for all sky imager based solar nowcasting, Sol. Energy 181 (2019) 251–263, https://doi.org/10.1016/j.solener.2019.02.004
[60] P. Ineichen, R. Perez, A new airmass independent formulation for the linke turbidity coefficient, Sol. Energy 73 (3) (2002) 151–157, https://doi.org/10.1016/S0038-092X(02)00045-2
[61] M. Schroedter-Homscheidt, M. Kosmale, S. Jung, J. Kleissl, Classifying ground-measured 1 minute temporal variability within hourly intervals for direct normal irradiances, Meteorol. Z. 27 (2018) 161–179, https://doi.org/10.1127/metz/2018/0875
[62] G. Nofuentes, C.A. Gueymard, J. Aguilera, M.D. Pérez-Godoy, F. Charte, Is the average photon energy a unique characteristic of the spectral distribution of global irradiance? Sol. Energy 149 (2017) 32–43, https://doi.org/10.1016/j.solener.2017.03.086
[63] K.S. Anderson, C.W. Hansen, W.F. Holmgren, A.R. Jensen, M.A. Mikofski, A. Driesse, Pvlib Python: 2023 project update, J. Open Source Softw. 8 (92) (2023) 5994, https://doi.org/10.21105/joss.05994
[64] A. Forstinger, S. Wilbert, A. Driesse, B. Kraas, Uncertainty calculation method for photodiode pyranometers, Sol. RRL 6 (5) (2022) 2100468, https://doi.org/10.1002/solr.202100468
[65] M.J. Prilliman, C.W. Hansen, J.M. Keith, S. Janzou, M. Theristis, A. Scheiner, E. Ozakyol, Quantifying Uncertainty in PV Energy Estimates Final Report, Report NREL/TP-7A40-84993, National Renewable Energy Laboratory (NREL), Golden, CO (United States), 2023. https://www.nrel.gov/docs/fy23osti/84993.pdf.
[66] suntrace GmbH, The Value of Measurements for Solar Energy Projects, Report, Hamburg, Germany Sep 2021. https://web.archive.org/web/20251008005538/https://dornier-group.com/app/uploads/sites/5/2021/09/White-Paper-Suntrace.pdf.
[67] Y. Fabel, N. Blum, B. Nouri, S. Wilbert, S. Gonzalez Rodriguez, L. Zarzalejo, SolarVision almería: a ground-based dataset of all-sky images, solar irradiance, and meteorological measurements, 2025. https://doi.org/10.1594/PANGAEA.980067
[68] Kipp&Zonen, CHP1 Pyrheliometer Instruction Manual, Report Manual version: 0811, Delft, The Netherlands, 2008. https://web.archive.org/web/20251007110157/https://www.kippzonen.com/Download/202/CHP-1-Pyrheliometer-Manual.
[69] Hukseflux Thermal Sensors, User Manual DR30-D1, Report manual v2305, Delft, The Netherlands, 2023. https://web.archive.org/web/20251007105943/https://www.hukseflux.com/uploads/product-documents/DR30-D1_manual_v2305.pdf.
[70] EKO INSTRUMENTS CO. LTD, MS-57 Pyrheliometer Manual Version 3, Report, Tokyo, Japan Apr 2019. https://web.archive.org/web/20251007092544/https://eko-instruments.com/asia/wp-content/uploads/sites/13/2024/08/ms-57-manual.pdf.
[71] D. Buie, A.G. Monger, C.J. Dey, Sunshape distributions for terrestrial solar simulations, Sol. Energy 74 (2) (2003) 113–122, https://doi.org/10.1016/S0038-092X(03)00125-7
[72] S. Wilbert, E. Guillot, Database with Frequencies of Circumsolar Ratio (CSR) Occurrence at Different Sites and Correlations of CSR with DNI and DHI Data, Report R13.6, SFERA Solar Facilities for the European Research Area, 2013.
[73] Y. Fabel, B. Nouri, S. Wilbert, N. Blum, R. Triebel, M. Hasenbalg, P. Kuhn, L.F. Zarzalejo, R. Pitz-Paal, Applying self-supervised learning for semantic cloud segmentation of all-sky images, Atmos. Meas. Tech. 15 (3) (2022) 797–809, https://doi.org/10.5194/amt-15-797-2022
[74] B. Nouri, S. Wilbert, P. Kuhn, N. Hanrieder, M. Schroedter-Homscheidt, A. Kazantzidis, L. Zarzalejo, P. Blanc, S. Kumar, N. Goswami, R. Shankar, R. Affolter, R. Pitz-Paal, Real-time uncertainty specification of all sky imager derived irradiance nowcasts, Remote Sens. 11 (9) (2019) 1059, https://doi.org/10.3390/rs11091059
[75] K. He, X. Zhang, S. Ren, J. Sun, Deep residual learning for image recognition, in: Proceedings of the IEEE Conference on Computer Vision and Pattern Recognition, 2016, pp. 770–778, https://doi.org/10.1109/CVPR.2016.90